Study on Seesaw-twisting System with Cylindrical Steel Slit Damper for Vibration Control of Steel Buildings

（建築鋼構造振動制御のための鋼製円筒スリットダンパーを用いたシーソー捻回システムに関する研究）

学位取得年月 **2024** 年 **3** 月

Shuai Feng

ACKNOWLEDGMENTS

First and foremost, I am extremely grateful to my supervisor, Professor Hiroshi Tagawa. His peace and respect make me feel truly educated. Three and a half years of doctoral studies have been like a magical journey, enriching the possibilities in my life. This experience will continue to support me in the days ahead. I would also like to thank the assistant professor, Dr. Xingchen Chen, for her technical support and interpersonal skills. Her selflessness and assistance to others have shown me another dimension of life, and I hope to carry what I've learned from her to make a greater contribution to society.

My deepest appreciation goes to the HU SPRING Research Grant Program, enabling me to invest more of my experiences into research and experience Japanese culture and scenery during my doctoral phase. The fresh atmosphere of Higashi-Hiroshima will remain in my memory forever. After my doctoral studies, feeling Hiroshima, a city I had previously only seen in English textbooks, as if it has become a part of me as well.

I would like to express my gratitude to my wife, who brought me to Japan and showed me a whole new world. In Japan, we jointly raised two children, which has been an unprecedented life experience. I would like to extend special thanks to my son and daughter. It's because of you that I had to visit pediatric clinics, amusement parks, aquariums, and countless other attractions, experiencing another university called society. Whenever I see the bright light in my son, I feel that life is filled with hope. Whenever I see my daughter playfully frolicking, I feel the richness of life.

Lastly, I would like to say that Japan's unique culture and art have greatly enriched my understanding of the world. I hope to contribute to the exchange between China and Japan in the future. Both Japan and China deserve to be understood by everyone.

ABSTRACT

This thesis aims to explore an innovative application of a seesaw-twisting system (STS) that incorporates a newly proposed cylindrical steel slit damper (CSSD) to dissipate seismic energy and enhance the seismic performance of structures. The proposed STS extends the conventional seesaw system and includes two steel rod braces, an upper member, a pin, a bottom member, and the CSSD. Within the seesaw-twisting system, the reciprocating structural vibrations are effectively transferred into the torsion of the CSSD, leading to elastoplastic flexural deformation of the strips created by the slits to dissipate seismic energy. The testing program for this study was performed to achieve the goals of this study between June 30th, 2021, and July 5th, 2021, at the Building Structure Laboratory of Hiroshima University. Each chapter of this dissertation summarizes the research conducted during the study period as follows.

Chapter 1 starts with a mechanism of the STS, which operates with a newly proposed CSSD and gives brief explanations of the yield mechanisms of the CSSD under the reciprocating structural vibration. In addition, the research innovation, the research objectives, and the scope of the dissertation are presented in this section.

In Chapter 2, the design of the proposed STS with CSSD is presented. In this chapter, an in-depth analysis of structural performance is conducted, focusing on the torsional stiffness and strength of CSSD, as well as the lateral stiffness and strength of STS.

In Chapter 3, the procedure of the displacement-controlled cyclic loading tests is presented to verify the system performance. Structural performance metrics, such as hysteretic behavior, energy dissipation capacity, strain distributions of the strip, cumulative plastic deformation capacity and failure form, were studied.

In Chapter 4, a numerical study was conducted to investigate the detailed stress distribution of the proposed CSSD. The FEA results exhibited hysteretic behavior that closely resembled the experimental data, and the FEA curves offered a similar prediction for the trend of the test skeleton curve and yield at nearly the same damper rotation angle.

In Chapter 5, the seismic performance of an STS was investigated using a three-story steel moment frame as a prototype building. Seismic response analyses, initially focusing on a typical STS configuration, involved examining peak inter-story drift angles under varying beam section, system stiffness and strength, and system specification. And additional frames with four distinct STS configurations were analyzed to examine the peak story drift angles and plastic hinge formation. The results showed that the STS with the CSSD efficiently reduced peak story drifts.

Chapter 6 summarizes the conclusions of this study in experimental and numerical study for STS with CSSD and seismic performance of steel structures with STS using CSSD. Furthermore, it highlights its future extended studies in these two research directions.

TABLE OF CONTENTS

LIST OF TABLES

LIST OF FIGURES

NOMENCLATURE

k_s : initial stiffness of one strip

S_D : initial torsional stiffness of the CSSD

F_s^P : plastic yield strength of one strip

T_D^P : torsional strength of the CSSD

E : Young's modulus of steel

G : Shear modulus of steel

M_P : full-plastic moment of the strip section

c : stiffness reduction factor

σ_y : steel material yield stress

n : number of strips in the device

l' : equivalent strip length

t : thickness of the strip

b : width of the strip

D : outer diameter of the damper section

δ : lateral displacement of the frame

f_R : magnification factor of the seesaw system

δ_D : vertical displacement of point A

δ_B : deformation of the brace

α : bracing angle

β : angle of line AO relative to the horizon

θ : torsional angle of the damper

w : lateral distance between points O and A

F_B : axial force applied to the brace in the test

k_B : axial stiffness of the brace

F : lateral force acting on the system in the test

T : torque moment exerted on the CSSD in the test

e : perpendicular distance from point O to the brace

k_{eval} : evaluated system initial lateral stiffness

F_y^{eval} : evaluated system lateral yield strength

$\boldsymbol{R}$: story drift angle

$\boldsymbol{\delta}$: lateral displacement of the frame

$\boldsymbol{h}$: frame height

$\boldsymbol{f}_{\mathrm{st}}^{\mathrm{e}}$: amplification factor of the seesaw-twisting system during the elastic stage

$\boldsymbol{f}_{\mathrm{st}}^{\mathrm{p}}$: amplification factor of the seesaw-twisting system where S_{D}=0

$\boldsymbol{\eta}$: cumulative plastic deformation ratio

${}_{\mathrm{cum}}\boldsymbol{\delta}_{\mathrm{p}}^{+}$: cumulative plastic deformation in the positive loading directions

${}_{\mathrm{cum}}\boldsymbol{\delta}_{\mathrm{p}}^{-}$: cumulative plastic deformation in the negative loading directions

$\boldsymbol{\delta}_{\mathrm{y}}$: lateral yield deformation of the frame

$\boldsymbol{K}_1$: elastic stiffness of the bi-linear model

$\boldsymbol{P}_{\mathrm{y}}$: initial lateral yield strength of bi-linear model

$\boldsymbol{c}_1$: isotropic hardening coefficient

$\boldsymbol{c}_2$: kinematic hardening coefficient

$\boldsymbol{E}_{\mathrm{total}}$: absolute disparity in total energy dissipation between the test and bi-linear model

$\boldsymbol{E}_{\mathrm{sum}}$: sum of absolute differences at amplitude points between the test and bi-linear model

$\boldsymbol{k}_{\mathrm{FEA}}$: system initial lateral stiffness from FEA

$\boldsymbol{F}_{\mathrm{y}}^{\mathrm{FEA}}$: system lateral yield strength from FEA

$\boldsymbol{k}_{\mathrm{test}}$: system initial lateral stiffness from tests

$\boldsymbol{F}_{\mathrm{y}}^{\mathrm{test}}$: system lateral yield strength from tests

$\boldsymbol{R}_{\mathrm{y}}^{\mathrm{eval}}$: evaluated system yield story drift angle

$\boldsymbol{R}_{\mathrm{y}}^{\mathrm{FEA}}$: system yield story drift angle from FEA

$\boldsymbol{R}_{\mathrm{y}}^{\mathrm{test}}$: system yield story drift angle from tests

ABBREVIATIONS

CSSD : Cylindrical steel slit damper

STS : Seesaw-twisting system

FEA : Finite element analysis

BF : Bare frame

MA : Model A

MB : Model B

MC : Model C

MD : Model D

ME : Model E

1. INTRODUCTION

1.1 Background

In recent decades, there has been a growing interest in structural control technologies for both new and retrofitted constructions, aimed at mitigating structural vibrations caused by dynamic loads [1].

A range of energy dissipation devices has been developed, encompassing metallic, frictional, viscoelastic, and fluid viscous dampers [2-6]. Notably, metallic dampers, specifically steel slit dampers, offer easy practical implementation as they do not necessitate specialized fabrication techniques or expensive materials [7-12]. Steel slit dampers, within the category of metallic dampers, are recognized for their effectiveness and reliability in reducing earthquake-induced damage in structures. Moreover, their behavior can be accurately forecast using straightforward formulas.

Chan and Albermani introduced a steel slit damper and explored the impact of geometric parameters on its behavior [13]. Subsequently, finite element analysis was employed to define appropriate slenderness ratios reflecting the buckling behavior of the damper [14], and a numerical model was utilized to determine the optimal boundary shape [15]. Ma et al. investigated the thin slit dampers under large shear deformation and butterfly dampers with various combinations of geometry and thickness through testing and numerical modeling techniques [16]. This paved the way for several applications of the damper. Saffari et al. integrated slit dampers at the bottom of beam flange plates to enhance the connection behavior between beams and columns [9]. Liu et al. innovatively designed a resilient rocking column, featuring replaceable steel slit dampers at the base, for rapid post-earthquake recovery [17]. As advancements continued, new types of slit dampers emerged. Amiri et al. proposed a novel block slit damper by increasing strip thickness [18], aiming to reduce inter-story drift ratios and absolute floor accelerations in steel moment frames [19]. Lee and Kim developed a box-shaped steel slit damper with four slit plates, generating substantial damping force within a compact size [20]. Naeem and Kim connected weak and strong slit dampers to create a multi-slit damper, assessing its effectiveness through a seismic performance comparison of a five-story ordinary moment frame before and after retrofitting [21]. Kim and Shin conducted three cyclic loading tests to validate a hybrid energy dissipation device incorporating a steel slit damper and friction pads [7]. Seo et al. combined a slit damper with shape memory alloy bending bars to enhance post-yield strength and energy dissipation [10]. The seismic performance of this hybrid device was further verified by incorporating it into a seven-story steel structure [22].

These slit dampers offer versatile installation options, including diagonal and chevron braces, as well as seesaw systems, for the dissipation of earthquake-induced energy within structures [23]. Previous research has particularly emphasized the effectiveness of the seesaw system. Investigations, both experimental and numerical, have been carried out on seesaw systems employing U-dampers,

steel slit dampers, and fluid viscous dampers [23-26]. Building upon these insights, seismic response analyses were extended to three- and six-story steel moment frames, both with and without the seesaw system [5-6]. Papagiannopoulos et al. [27] delved into the seismic response of a series of low-rise plane steel frames, exploring three different configurations of the seesaw system and extracting peak drift ratios. Subsequent studies [28-29] extended this exploration to two-, five-, and eight-story 3-D steel structures, incorporating the seesaw system and subjecting them to diverse seismic motions through inelastic seismic time-history analyses. Furthermore, the viability of applying the seesaw system as a seismic retrofitting method for older, nonductile reinforced concrete buildings was confirmed [24].

Nonetheless, the torsional potential of the seesaw component remains untapped, and the energy dissipation of steel slit dampers is restricted to planar motion. In light of these constraints and the need for advancement in these specific directions, the research in this study will be elaborated upon in the subsequent sections.

1.2 Research innovation

Illustrated in **Fig. 1.1** is the arrangement of the newly proposed cylindrical steel slit damper (CSSD). This design is constructed using a steel cylinder with end plates welded at both terminations. The cylinder features a set of slits longitudinal cut, resulting in a defined number of strips. These slits incorporate rounded ends, effectively mitigating stress concentration at the strip extremities. Additionally, bolt holes are meticulously drilled into each end plate to facilitate seamless connection to the system. This approach not only circumvents on-site welding, minimizing uncertainties associated with fieldwork but also allows for straightforward replacements.

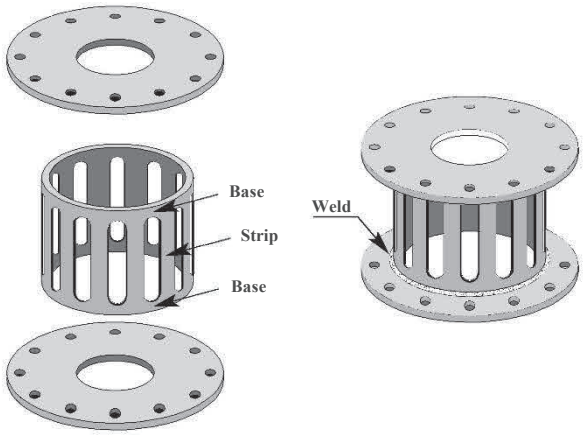

Fig. 1.1. Geometric design of cylindrical steel slit damper.

Displayed in **Fig. 1.2** is the innovative seesaw-twisting energy dissipation system (STS), comprising two steel rod braces, an upper member, a pin, a bottom member, and the novel CSSD.

The damper is affixed on one side to the stationary bottom member, while the opposite side is linked to the freely rotatable upper member. A pivotal pin traverses through these components, functioning as both the torsion center for the upper member and the CSSD. This pin bears the shear force transmitted through the seesaw-twisting system, with its magnitude equating the lateral load. Given the potential for brittle shear failure of the pin and the reinforcing impact of the CSSD, a safety factor exceeding three is recommended in pin design [27].

Each edge of the upper member is connected to a frame vertex by a diagonal rod brace, composed of steel rods equipped with turnbuckles. The introduction of pre-tension in the rods through turnbuckles aligns with the seesaw system's property, ensuring that only tensile forces appear in the bracing members during vibrations. As depicted in **Fig. 1.2**(b), a rightward lateral force (F) induces lateral displacement, triggering the twisting of the upper member via two braces. Consequently, the CSSD undergoes torsional deformation, leading to flexural deformation in each strip. The plastic deformation of these steel strips effectively dissipates seismic energy, mitigating structural responses. Conversely, a leftward load prompts the opposite rotation of the upper member, inducing reverse bending deformation in the strips. This reciprocal vibration transforms into elastoplastic deformation in the CSSD.

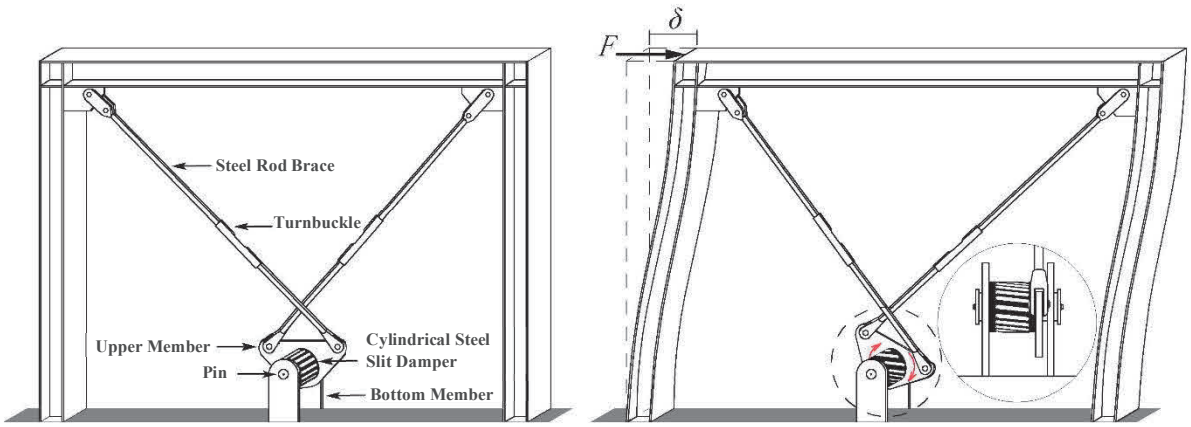

Fig. 1.2. Concept of seesaw-twisting system with cylindrical steel slit damper:
(a) initial configuration; (b) deformed configuration.

1.3 Research objectives

In general, this research consists of two objectives.

The first objective focuses on the newly raised STS with CSSD, scrutinizing not only its configuration but also delving into its mechanical characteristics. The investigative approach involves a series of five cyclic loading tests, meticulously conducted to extract valuable insights into the

system's hysteretic performance and the underlying patterns of failure. A detailed visualization of the stress distribution within the proposed CSSD was provided by the numerical study.

The second objective aimed to investigate further the seismic performance of the proposed system by incorporating it into a three-story steel prototype building. An analysis was conducted on both a typical STS configuration and four distinct configurations to scrutinize the peak story drift angles and the formation of plastic hinges. The impact of the amplification factor on the seismic response of frames with varied configurations was thoroughly discussed. The outcomes revealed that the incorporation of CSSD in the STS effectively mitigated peak story drifts.

1.4 Scope

This dissertation encompasses two stages in the research program.

In the initial phase, an extension of the seesaw system was introduced, transforming it into a twisting device, denoted as the seesaw-twisting system, as depicted in **Fig. 1.2**. This system integrates a novel CSSD designed to dissipate energy in response to story drift. The primary focus lies in the comprehensive examination of the configuration and mechanical attributes of both the newly raised CSSD and the STS. Initial lateral stiffness and lateral yield strength formulas are derived, and their validity is examined. The assessment encompasses the verification of hysteretic performance and energy dissipation capacity through a series of five cyclic tests. The test data is used to scrutinize the validity of the evaluation formulas and finite element analyses for the initial stiffness and yield strength of the proposed system. A concise bi-linear model is then employed to characterize the proposed system, and its accuracy is affirmed by comparing it with experimental results. To further delve into the system's behavior, finite element analyses are conducted, depicting the detailed stress distribution characteristics of the damper.

In the second phase, the aim was to investigate further the seismic performance of the proposed system by incorporating it into a three-story steel prototype building. This investigation focused initially on a representative STS configuration, where displacement time-history responses at the top floor were meticulously generated using OpenSees. The assessment extended to evaluating maximum inter-story drift angles under varying conditions, including system stiffness and strength, beam section specifications, and alterations in the system configuration. Following this, comprehensive seismic response analyses were carried out for models featuring one typical STS configuration and four distinct arrangements. This extensive evaluation included an examination of peak story drift angles, the operational status of the CSSD, and the formation of plastic hinges.

1.5 Dissertation outline

Illustrated in **Fig. 1.3**, the study introduced the seesaw-twisting system with CSSD following the introduction. The investigation into the system's attributes was conducted through cyclic loading tests, numerical analysis, and an exploration of the seismic performance of steel structures equipped with STS utilizing CSSD. With the core research content as the foundation, this dissertation is organized into the subsequent chapters:

Chapter 1 commences with an overview of the role of steel slit dampers and seesaw systems in structural control technologies, emphasizing their significance in mitigating structural vibrations under dynamic loads. Furthermore, this chapter provides concise explanations of the newly proposed seesaw-twisting system with CSSD. Additionally, the section highlights the research's innovative aspects, outlines the objectives, and delineates the scope of the dissertation.

Chapter 2 proposes the design concept of the seesaw-twisting system with CSSD. In this regard, evaluation formulas for the torsional stiffness and strength of CSSD and lateral stiffness and strength of STS was derived. Additionally, the relationship between the story drift angle and CSSD torsional angle was derived in this section.

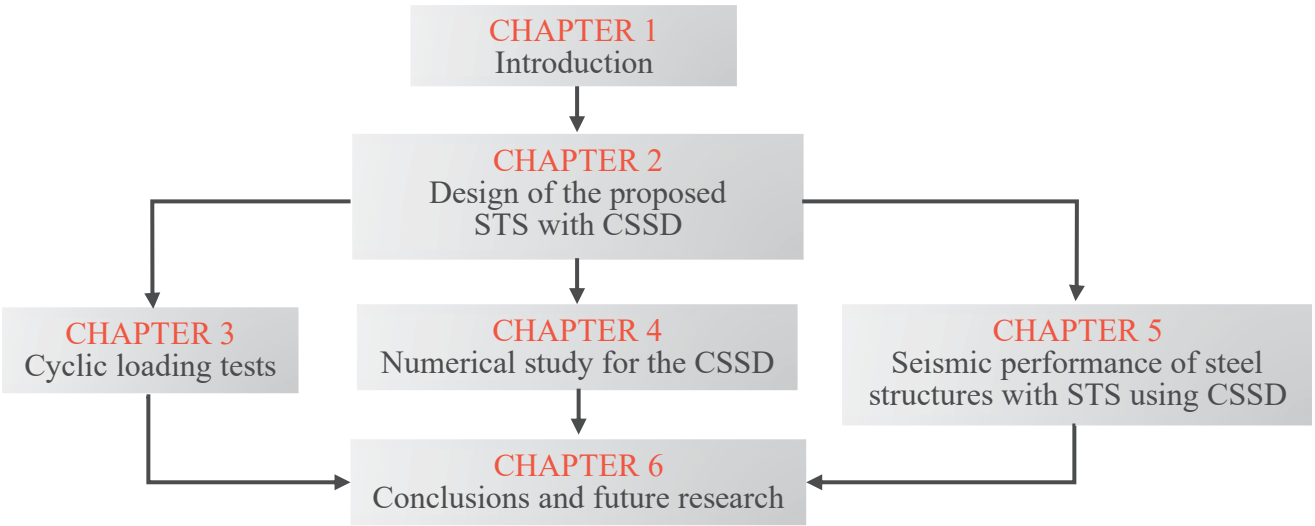

Fig. 1.3. Flowchart of chapter dissertation structure.

Chapter 3 presents the cyclic loading tests aimed at scrutinizing the performance of the proposed STS with CSSD. Specifically, three cyclic loading tests featuring increasing amplitudes and two tests with constant amplitudes were executed. Notably, the tests revealed a uniform conversion of torque moment to the tangential force in each strip of the CSSD during loading. The system exhibited remarkably stable hysteretic characteristics and showcased a substantial capacity for energy dissipation. Moreover, all dampers entered plastic deformation at a small story drift angle, indicating their early yielding during seismic events for effective energy dissipation. The experimental specimens demonstrated resilience, with failure only occurring after enduring numerous loading

cycles, showcasing an exceptional plastic deformation capacity. The force-deformation relation of the proposed system can be fitted into a brief bi-linear model, through which both the hysteretic curve and dissipated energy can be accurately described.

Chapter 4 introduces a numerical investigation through finite element analysis, aimed at exploring the detailed stress distribution within the proposed CSSD. To achieve this, the section employs both hysteretic and one-directional loading analyses provided by ANSYS. Additionally, the chapter offers comprehensive explanations of the finite element analysis parameters and results. In terms of the initial lateral stiffness and lateral yield strength, the system's performance, as described by both theoretical considerations and finite element analysis, exhibited a satisfactory alignment with the experimental results.

Chapter 5 investigated the seismic performance of an STS using a three-story steel moment frame as a prototype building. Initial seismic response analyses were centered around a typical STS configuration. The examination encompassed peak inter-story drift angles under various conditions, including alterations in beam sections, system stiffness and strength, and system specifications. Furthermore, analyses of frames with four distinct STS configurations were undertaken to assess peak story drift angles and plastic hinge formation. Based on the analysis results, the effect of the amplification factor on the seismic response of the frame with diverse configurations was discussed. The outcomes underscored the efficacy of the STS with CSSD in significantly reducing peak story drifts.

Chapter 6 summarizes the conclusions of this entire study within two subsections and offers suggestions for further inquiry investigations because future research is highly needed to extend this study. These potentials of STS collaboratively working with other torsional dampers, such as hydraulic dampers, friction dampers, etc. are worth exploring in future theoretical and experimental studies. To advance the practical application of STS with CSSD, forthcoming research should delve into the development of an equivalent simplified damper for the system and establish design criteria for its optimal implementation.

2. DESIGN OF THE PROPOSED STS WITH CSSD

This chapter describes the design conception and theory of the proposed STS with CSSD. The seesaw system has been extended to serve as a torsional device, now referred to as the seesaw-twisting system (STS), which functions with a newly proposed cylindrical steel slit damper (CSSD) to dissipate energy under story drift. The chapter commences by examining the configuration and mechanical characteristics of the newly raised CSSD and STS. Subsequently, attention is turned to articulating the initial torsional stiffness and torsional strength of the CSSD. Utilizing the characteristics of the CSSD and accounting for geometric deformations, formulas are developed to assess the initial lateral stiffness and lateral yield strength of the overall system.

2.1 Outline of the proposed STS with CSSD

In **Fig. 2.1**(a), the configuration of the newly proposed CSSD is depicted. This damper is constructed using a steel cylinder with welded end plates at both ends. A series of slits are cut from the cylinder, resulting in a specific number of strips. The slits feature rounded ends, alleviating stress concentration at the edges of the strips. Bolt holes are positioned on each end plate, facilitating system connection. This design choice eliminates the need for on-site welding, mitigating uncertainties associated with fieldwork and ensuring straightforward replacement.

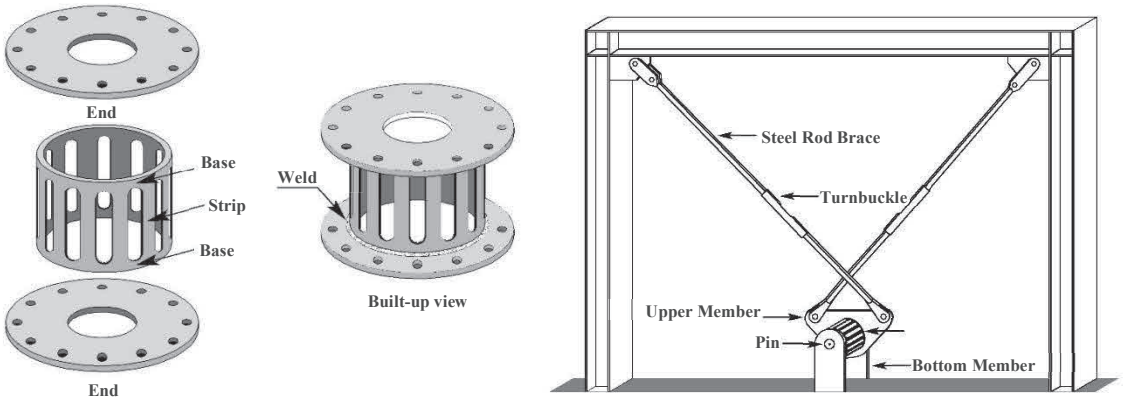

(a) (b)

Fig. 2.1. Cylindrical steel slit damper (CSSD) and seesaw-twisting system (STS): (a) geometric design of the CSSD, (b) concept of STS.

In **Fig. 2.1**(b), the proposed seesaw-twisting energy dissipation system is illustrated, consisting of two steel rod braces, an upper member, a pin, a bottom member, and the innovative CSSD. One end of the damper is screwed to the stationary bottom member, while the other end is affixed to the freely rotatable upper member. The pin traverses through these components, serving as both the torsion center for the upper member and the CSSD. This pin endures the shear force transmitted through the

seesaw-twisting system, with the magnitude of the shear force equating to the lateral load. To account for the brittle shear failure potential of the pin and the hardening effect of the CSSD, the safety factor in pin design should exceed three, as recommended in [30]. Each extremity of the upper member is linked to a frame vertex by a diagonal rod brace. These braces, constructed from steel rods with turnbuckles, allow the introduction of pre-tension, ensuring that only tensile forces manifest in the bracing members during vibration. Because the CSSD damper is installed on the bottom member for protection and the steel rod braces can move freely out of the plane, the STS system can still function as usual even in the presence of out-of-plane motion.

As depicted in **Fig. 2.2**, the application of a rightward lateral force F induces lateral displacement, triggering the rotation of the upper member through two braces. Simultaneously, the CSSD undergoes torsional twisting, leading to flexural deformation in each strip. The seismic energy is dissipated through the plastic deformation of the steel strips, effectively diminishing structural responses. Conversely, a leftward load initiates the opposite rotation of the upper member, causing reverse bending deformation in the strips. Consequently, the reciprocating vibration of the structure is converted into elastoplastic deformation within the CSSD.

When subjected to lateral loads, the frame undergoes deformation, inducing torsional changes in the CSSD and effectively reducing seismic structural responses. During seismic events, the STS transforms the structure's reciprocating vibration into plastic torsional deformation of the CSSD, contributing to the alleviation of seismic structural responses and the dissipation of energy. In principle, the CSSD should not yield under wind loads. However, there might be allowances for dampers to enter the plastic range under wind loads, as long as essential structural elements like columns and beams remain within their elastic limits and the damper's performance doesn't deteriorate due to repeated deformation [31].

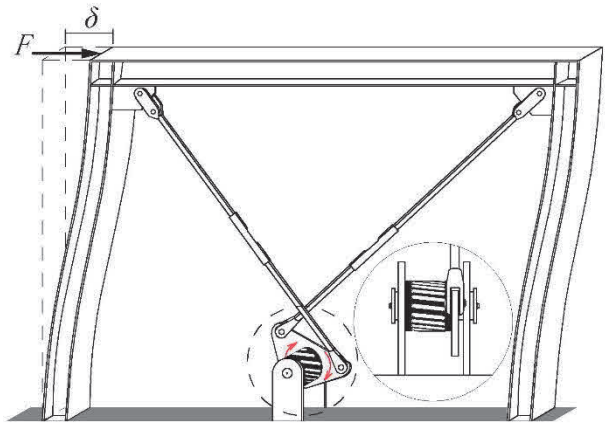

Fig. 2.2. STS under a rightward load.

2.2 Theory of the proposed STS with CSSD

2.2.1 Torsional Stiffness and Strength of CSSD

As the two end plates undergo relative rotation, the strips exhibit behavior of beams anchored on one side and supported on the opposite end by a roller. When subjected to a lateral force F_s, each strip undergoes bending, showcasing an inflection point at its midpoint (refer to **Fig. 2.3**(c)). Additionally, there is a subtle deformation in the bases. The moment experienced by each strip follows a linear increment from the midpoint towards the two ends (as depicted in **Fig. 2.3**(d)). With a significant relative rotation of the two end plates, plastic hinges materialize at each strip's end. The tangential bearing forces of the circularly arranged strips contribute to the CSSD bearing torque.

The initial stiffness of each strip, denoted as k_s, and the initial torsional stiffness of the CSSD, represented by S_D, are mathematically defined as follows:

$$k_s = \frac{1}{\frac{l'^3}{Etb^3} + \frac{l'}{Gtb}} \tag{2.1}$$

$$S_D = cnk_s(\frac{D-t}{2})^2 \tag{2.2}$$

The plastic yield strength of each strip, denoted as F_s^P, and the torsional strength of the CSSD, expressed as T_D^P, are derived as follows:

$$F_s^P = \frac{2M_P}{l'} = \frac{\sigma_y tb^2}{2l'} \tag{2.3}$$

$$T_D^P = nF_s^P \frac{D-t}{2} \tag{2.4}$$

In the given context, where E denotes Young's modulus, G represents the shear modulus, M_P signifies the full-plastic moment of the strip section, c is a stiffness reduction factor expressed as a fraction of the fixed-ended stiffness, to be determined through experimentation, σ_y denotes the material yield stress, and n represents the number of strips in the device. The symbol l' corresponds to the equivalent strip length [32-33], as illustrated in **Fig. 2.3**(b). Additionally, t and b denote the thickness and width of the strip, respectively, and D represents the outer diameter of the damper section, as shown in **Fig. 2.3**(a).

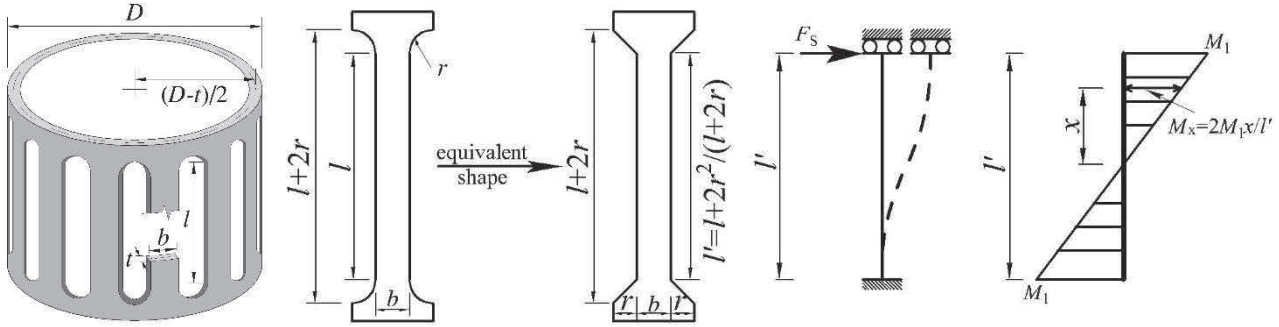

Fig. 2.3. Geometric parameters of the CSSD and single strip:
(a) geometric parameters of the CSSD, (b) equivalent strip length,
(c) deformed configuration of a single strip, (d) bending moment distribution.

2.2.2 Lateral stiffness and strength of STS

Illustrated in **Fig. 2.4** is a simplified analysis model. Points A and B symbolize the left and right connection points of the upper member and two braces, respectively. Point O denotes the center of the pin as well as the damper. Concerning geometric deformation, the interplay of displacements δ, δ_D, and δ_B can be expressed through the relationship [6]:

$$\delta = \frac{\delta_D}{f_R} + \frac{\delta_B}{\cos\alpha} \tag{2.5}$$

where δ represents the lateral displacement of the frame, f_R denotes the magnification factor of the seesaw system, and δ_D corresponds to the vertical displacement of point A. The parameter δ_B is the deformation of the brace, these parameters can be articulated as:

$$f_R = \frac{\cos\alpha\cos\beta}{\sin(\alpha+\beta)} \tag{2.6}$$

$$\delta_D = \theta w \tag{2.7}$$

$$\delta_B = \frac{F_B}{k_B} \tag{2.8}$$

where α symbolizes the bracing angle, β denotes the angle of line AO relative to the horizon, θ represents the torsional angle of the damper, w is the lateral distance between points O and A as depicted in **Fig. 2.4**(a), F_B signifies the axial force applied to the brace, and k_B stands for the axial stiffness of the brace, as illustrated in **Fig. 2.4**(b).

The force relationships are:

$$F = 2F_B\cos\alpha \tag{2.9}$$

$$T = 2F_B e \tag{2.10}$$

where F symbolizes the lateral force acting on the system, T represents the torque moment exerted on the CSSD, and e denotes the perpendicular distance from point O to the brace.

From Eqs. (2.5)– (2.10), the system initial lateral stiffness k_{eval} can be obtained as:

$$k_{\text{eval}} = \frac{F}{\delta} = \frac{f_{\text{R}}\cos\alpha}{\frac{1}{S_{\text{D}}}we + \frac{1}{2k_{\text{B}}}\frac{f_{\text{R}}}{\cos\alpha}} \tag{2.11}$$

From Eqs. (2.3), (2.4), (2.9), and (2.10), the lateral yield strength $F_{\text{y}}^{\text{eval}}$ can be obtained as:

$$F_{\text{y}}^{\text{eval}} = \frac{T_{\text{D}}^{\text{P}}}{e}\cos\alpha = \frac{n\sigma_y t b^2 (D-t)\cos\alpha}{4l'e} \tag{2.12}$$

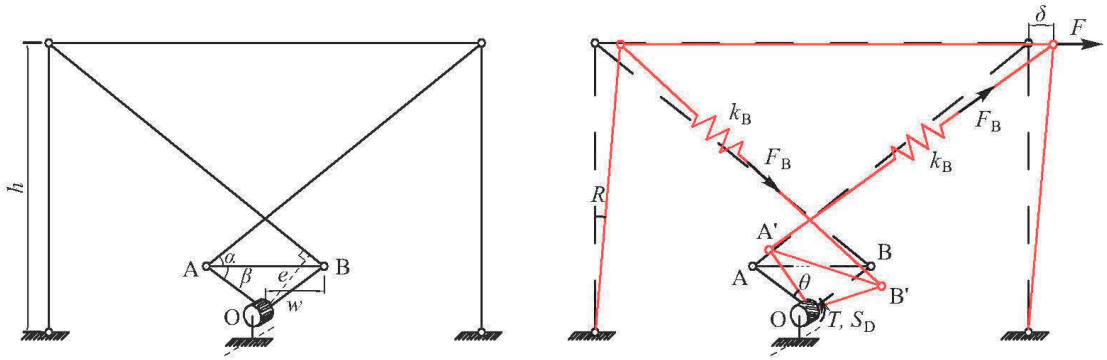

(a) (b)

Fig. 2.4. Simplified analytical model: (a) initial configuration, (b) deformed configuration.

2.2.3 Relationship between the story drift angle and CSSD torsional angle

As depicted in **Fig. 2.4**, the story drift induces torsional deformation in the CSSD through the proposed seesaw-twisting system. The amplification factor of the seesaw-twisting system is defined as the ratio of the CSSD's torsional deformation angle, θ, to the story drift angle, R.

In the realm of elastic deformation, the torsional deformation of the CSSD can be articulated by the torque moment T and the initial torsional stiffness S_{D}, expressed as:

$$\theta = \frac{T}{S_{\text{D}}} \tag{2.13}$$

The story drift angle, denoted as R, can be demonstrated in terms of the lateral displacement of the frame, δ, and the frame height, h, through the following expression:

$$R = \frac{\delta}{h} \tag{2.14}$$

From Eqs. (2.5), (2.7), (2.8), (2.10), and (2.13), the relationship between the lateral displacement of frame δ and the vertical displacement of point A δ_{D} can be obtained as follows:

$$\delta_{\text{D}} = \frac{1}{\frac{1}{f_{\text{R}}} + \frac{1}{2ewc\text{os}\alpha}\frac{S_D}{k_B}}\delta \tag{2.15}$$

By substituting Eqs. (2.7) and (2.14) into (2.15), the torsional angle of the damper θ can be expressed by the story drift angle R as follows:

$$\theta = \frac{1}{\frac{w}{f_{\mathrm{R}}h} + \frac{1}{2ehcos\alpha}\frac{S_{\mathrm{D}}}{k_{\mathrm{B}}}} R = f_{\mathrm{st}}^{\mathrm{e}} R \tag{2.16}$$

where $f_{\mathrm{st}}^{\mathrm{e}}$ denotes the amplification factor of the seesaw-twisting system during the elastic stage.

The amplification factor $f_{\mathrm{st}}^{\mathrm{e}}$ operates in conjunction with the stiffness ratio of the CSSD, S_{D}, and the braces, k_{B}. In the plastic range, where the stiffness S_{D} diminishes, and as the extreme case for S_{D}=0, Eq. (2.16) can be streamlined to:

$$\theta = \frac{f_{\mathrm{R}}h}{w} R = f_{\mathrm{st}}^{\mathrm{p}} R \tag{2.17}$$

3. CYCLIC LOADING TESTS

3.1 General

This chapter introduces five cyclic loading tests designed to validate the hysteretic performance and energy dissipation of the STS with CSSD. The initial interpretation encompasses the testing setup, test specimens, data measurement during testing, and the loading programs employed.

Following the introduction, the relationship between lateral load and story drift angle is depicted. Subsequent sections conduct the analysis of system deformation and brace behavior, followed by an in-depth examination of strip behavior. The scrutiny extends to the cumulative plastic deformation capacity and the observed failure form. To simulate the hysteretic behavior of the proposed system, a bi-linear hysteretic model is then introduced. This model demonstrates a high level of validity when compared to the test results, particularly in terms of the hysteretic curve and energy dissipation.

3.2 Testing setup

Fig. 3.1 and **3.2** visually depict the configuration of the conducted tests. Unlike viscous dampers, which are sensitive to temperature fluctuations, the steel slit damper exhibits minimal temperature dependency. Apart from that, the book of Recommended provisions for Seismic Damping Systems applied to Steel Structures [33] describes that the influence of the strain rate is slight when the steel materials except low yield point steel are adopted. The most crucial factor affecting the performance of the slit damper is its configuration. Hence, in this study, hysteresis loading was conducted on STS system with CSSDs of three different specifications. The framework, featuring full hinge connections, was attached utilizing a seesaw-twisting system comprising steel rod braces, an upper member (highlighted in green), a bottom member (highlighted in red), and the CSSD. As a result, the lateral stiffness and strength were exclusively contingent on the seesaw-twisting system. It is noteworthy to mention that this damping system is also applicable to the moment frame. The column and beam sections adopted the dimensions H-150×150×7×10, with a steel grade of SN400B. Notably, the out-of-plane displacement of the frame was constrained by a substantial fixed support frame positioned at the tops of the columns. As depicted in **Fig. 3.2**, there was a certain interval between the frame and the boundary frame at the initial stage of loading. To mitigate the friction between the boundary frame and the frame upon contact during the loading tests, a pair of rollers was affixed to the column top. The frame had a span and height of 2200 mm and 1568 mm, respectively. The bottom member, securely attached to the base beam, functioned as the base. It featured a pin with a diameter of 80 mm passing through it, serving as the torsion center for the upper member equipped with the damper.

As depicted in **Fig. 3.1**(b), one end of the innovative damper was affixed to the immobile bottom member, while the other end was attached to the upper member, enabling unrestricted rotation with the damper specimen around the pin. This rotation occurred in response to the reciprocating traction exerted by the braces. The upper member possessed the ability to move freely along the pin, preventing the increment of tension force in each strip of the CSSD. The deliberate omission of in-situ welding during damper installation was a strategic choice, facilitating effortless replacement post a significant seismic event. To ensure stability in torsion and to prevent warping, a support member parallel to the upper member was introduced. Each edge of the upper member was linked to the opposing beam-column joint via a single brace, featuring an axial stiffness of 13.3 kN/mm.

For the notations presented in **Fig. 2.4**, the values assigned were 300 mm for w, 364 mm for e, with the horizontal angles α and β measuring 42° and 36°, respectively. To prevent contact at the intersection of the bracing members, a cross-buckle component was employed. The brace members were constructed from steel rods of grade SS400 with a diameter of 25 mm. Monitoring of the brace axial force was achieved through strain gauges positioned on both sides near the upper edge. Connectivity of the steel rods was facilitated by turnbuckles, introducing a pre-tension of 20 kN equivalent to 200 μ strain to maintain the brace in a tensile state throughout the experiment. The effectiveness of pre-tension in practical applications, specifically in a seesaw system, was proven effective in a prior full-scale test utilizing a real-size three-story building [34]. This study utilized 38 mm diameter rods, noting minimal pre-tension loss during vibration tests over a rather long period of time. In that test, a dedicated tool was utilized for introducing pre-tension into the rods, instead of turnbuckle components.

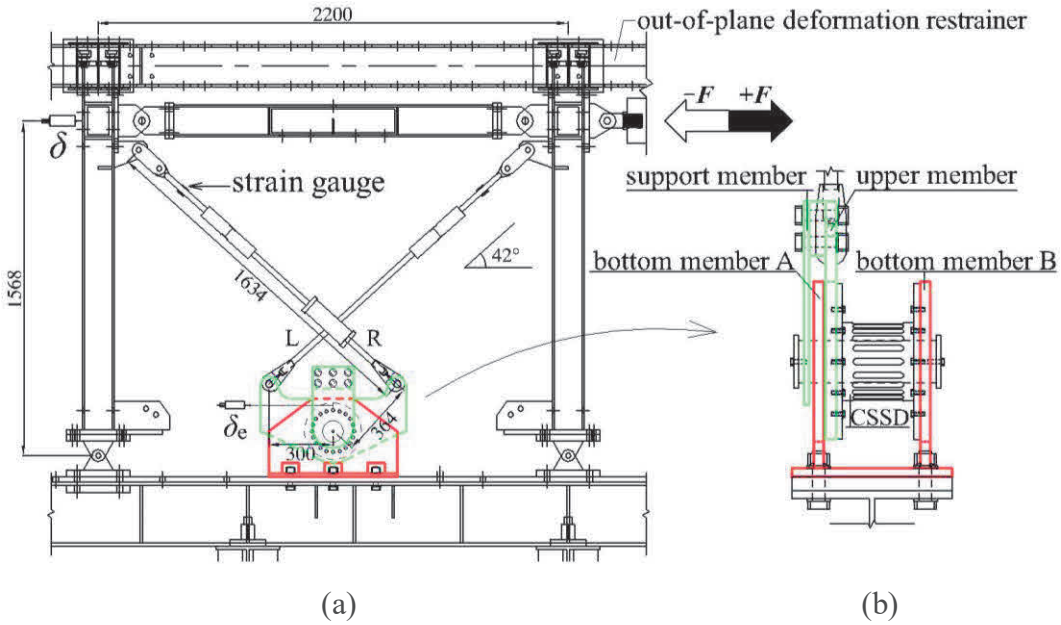

(a) (b)

Fig. 3.1. Test setup: (a) elevation; (b) damper details. (units: mm)

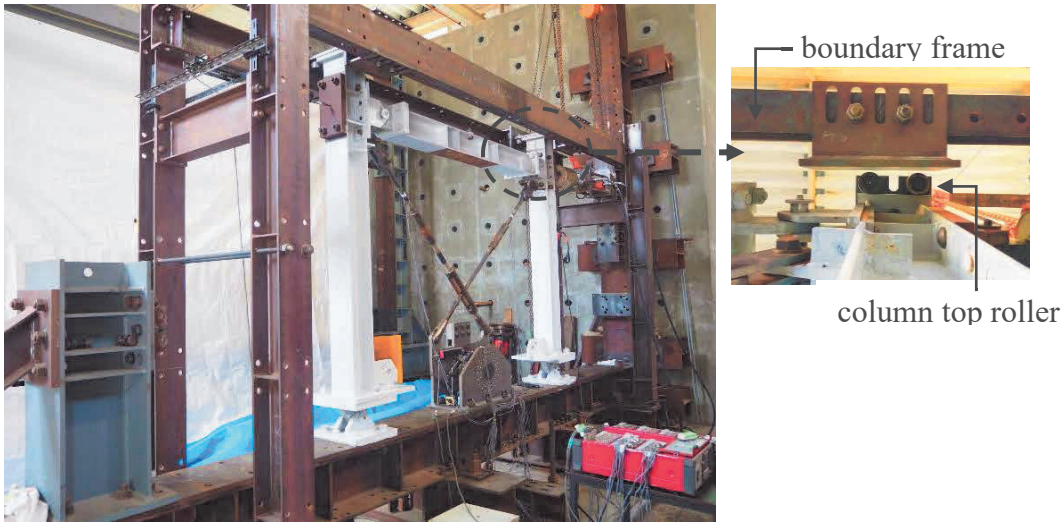

Fig. 3.2. Overall view of test setup and column top rollers.

3.3 Test specimens

The configuration and specifications of the CSSD in this experimental study are illustrated in **Fig. 3.3** and **Table 1**, respectively. The geometric quantities corresponding to each notation are elucidated in **Fig. 2.3**(a). The cylinder section was constructed from steel grade STKM13A, while the end plates were crafted from steel grade SS400. The column l'/b denotes the aspect ratio of the strip. Uniform in diameter and thickness, all dampers shared identical dimensions.

In this study, four specimens were fabricated. Specimens T-A and T-A-c shared the same configuration and served as the base models. In comparison, specimen T-B featured shorter strips, while specimen T-C boasted wider strips of nearly the same length as the base model. Each damper weighed approximately 11.5 kg. Six strain gauges, labeled T1-T6, B1-B6, L1-L6, R1-R6, were affixed to four strips in a predetermined order for each specimen. All specimens were composed of the same material, and the properties derived from tensile coupon tests were as follows: yield stress of 267 N/mm², ultimate stress of 472 N/mm², and elongation of 39%.

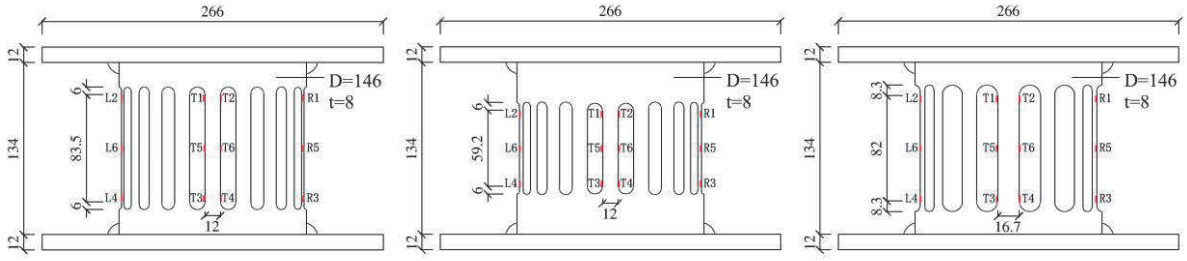

(a) Specimen T-A/ T-A-c (b) Specimen T-B (c) Specimen T-C

Fig. 3.3. Damper dimensions. (units: mm)

Table 1 – Damper specifications (units: mm)

Specimen	*D*	*t*	*l*	*b*	*l′*	*l′/b*	*n*	Loading amplitude
T-A	146	8	83.5	12.0	84.3	7	18	increasing
T-A-c	146	8	83.5	12.0	84.3	7	18	constant
T-B	146	8	59.2	12.0	60.2	5	18	increasing
T-C	146	8	82.0	16.7	83.4	5	13	increasing
T-N	—	—	—	—	—	—	—	constant

3.4 Testing data measurement

A single displacement sensor was strategically positioned on the end plate to precisely gauge and record the torsional angle of the CSSD. Furthermore, in the case of each specimen, an arrangement of six strain gauges was precisely applied onto four distinct strips. These strain gauges were specifically designated as T1-T6, B1-B6, L1-L6, and R1-R6, serving the essential purpose of measuring the axial deformation at both the root and middle sections of the strips. This deliberate placement ensured a comprehensive assessment of the structural response at critical points. Simultaneously, the lateral displacement, denoted as δ, was diligently measured, as visually depicted in **Fig. 3.1**, providing a comprehensive understanding of the lateral behavior and structural performance of the system under investigation.

3.5 Loading programs

A lateral force denoted as F was applied at the right beam-to-column connection, with rightward loading and displacement defined as positive in the conducted test. The loading schemes employed in this research are visually outlined in **Fig. 3.4**. For specimens T-A, T-B, and T-C, a loading regimen featuring gradually increasing amplitudes was implemented to scrutinize the hysteretic behavior of the designated damper. This involved incrementing the story drift angle R (=δ/1568 mm) from 0.005 to 0.04 at intervals of 0.005, with two complete loading cycles executed at each amplitude angle.

Conversely, a loading test employing a constant amplitude was conducted for T-A-c until its strength deteriorated to half of the initial value. This specific test aimed to elucidate the failure mode, cumulative plastic deformation, and dissipated energy of the device. Adhering to FEMA-461 [35] guidelines for quasistatic cyclic loading tests, the loading amplitude for this innovative damper was set at 0.03 rad. Notably, this amplitude of 0.03 rad was 8.6 times greater than the yield story drift angle of 0.0035 rad, as indicated in **Table 4**. Additionally, a two-cycle loading test with a constant amplitude of 0.04 rad was conducted for specimen T-N, which was without a damper, to assess the frictional resistance of the system. In the loading test for specimen T-N, an equivalent amount of pre-

tension was applied to the braces to replicate the experimental conditions employed for specimens T-A, T-B, and T-C.

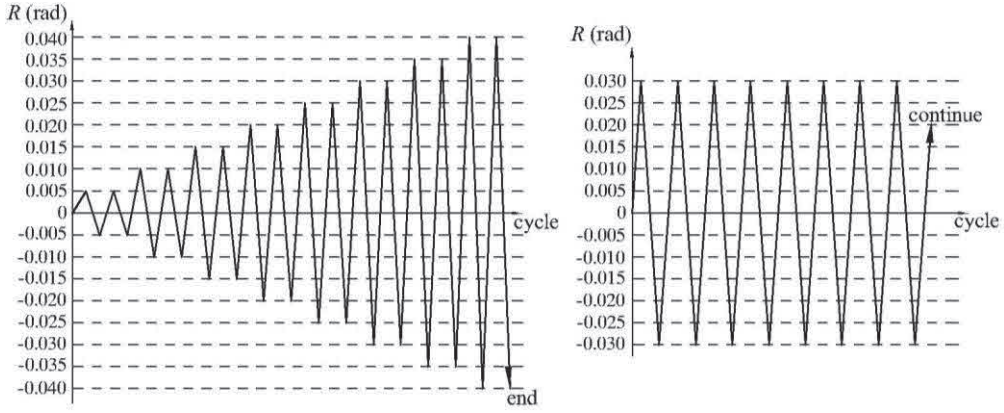

(a) (b)

Fig. 3.4. Loading history: (a) increasing amplitude; (b) constant amplitude.

3.6 Test results

3.6.1 Lateral load and story drift angle relationships

Fig. 3.5 illustrates the correlations between lateral load and story drift angle for specimens T-A, T-B, T-C, and T-N. Throughout the escalating amplitude loading tests, all CSSD specimens exhibited stable hysteretic properties, maintaining stability even when the maximum story drift angles reached 0.04 rad. Notably, specimens T-B, characterized by shorter strips, and T-C, with wider strips, displayed overall larger lateral loads compared to the base model T-A. The hysteresis curves for all specimens took on a plump spindle shape throughout the entire loading process, with a minimal increase in tension force observed in the strips.

In **Fig. 3.5**(d), the mechanical performance of the seesaw-twisting system without a damper is portrayed. At the yield story drift angle, the lateral load exhibited fluctuations around 1.2 kN, leading to the assumption that the frictional resistance of the system is approximately 1.2 kN. This value is crucial for determining the $F_{\mathrm{y}}^{\mathrm{test}}$ values in Table 3 and P_{y} in the bi-linear model. It's important to note that all experimental curves in the figures are derived from raw data.

The measured initial lateral stiffness (k_{test}) in the conducted tests were 1.28 kN/mm, 2.88 kN/mm, and 2.12 kN/mm, respectively. Correspondingly, the lateral yield strengths $F_{\mathrm{y}}^{\mathrm{test}}$ were determined to be 4.86 kN, 7.16 kN, and 7.51 kN. The calculation of lateral yield strength involved identifying the lateral load at which the lateral stiffness decreased to one-third of its initial value, accounting for a frictional resistance of 1.2 kN.

In the early phases of the loading processes, all specimens exhibited yielding at approximately R=0.003 rad. The measured yield story drift angles R_y^{test} were recorded at 0.0035 rad, 0.0022 rad, and 0.0030 rad, respectively.

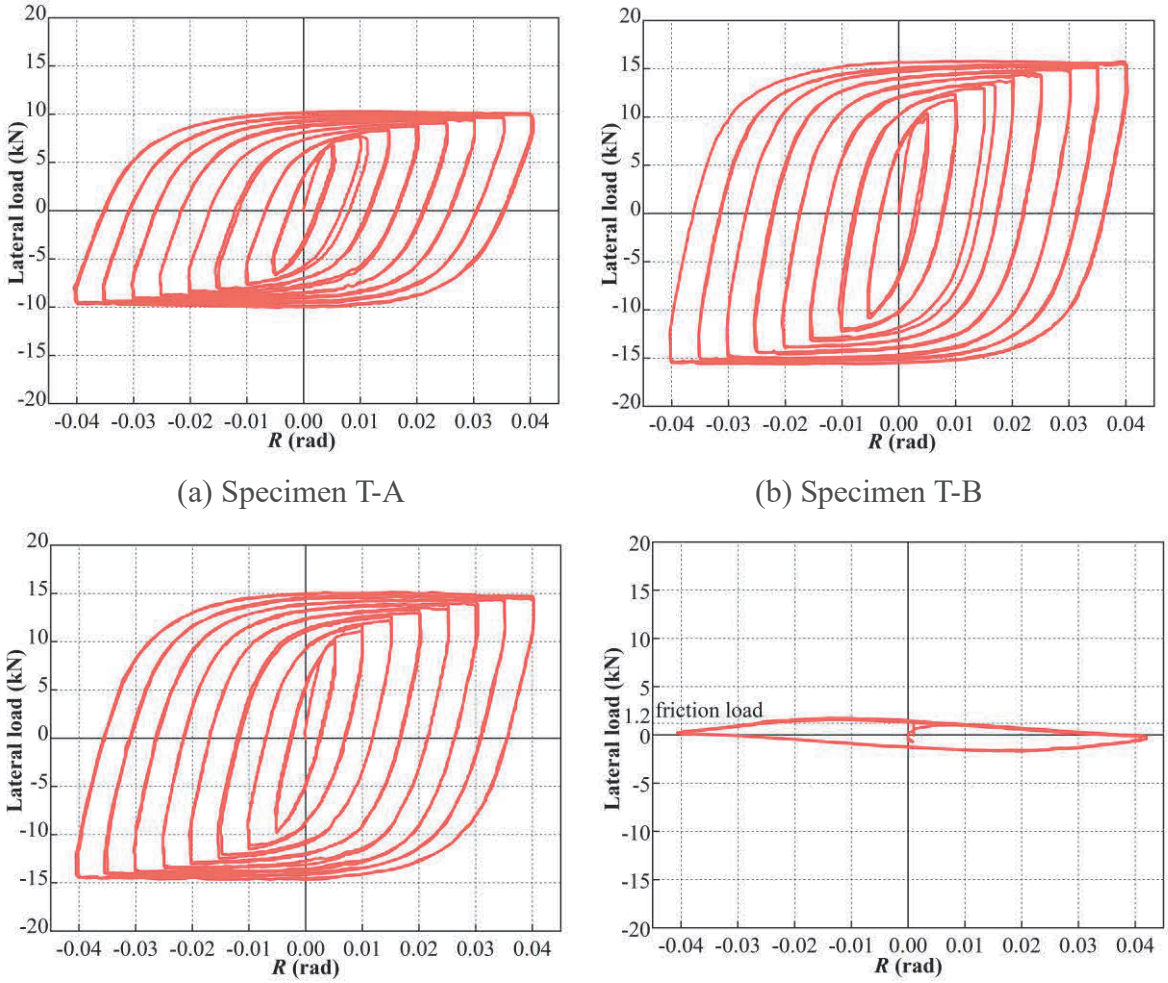

(a) Specimen T-A (b) Specimen T-B

(c) Specimen T-C (d) Specimen T-N.

Fig. 3.5. Lateral load and story drift angle relationships.

3.6.2 System deformation and brace behavior

The deformations of the entire system, upper member, and damper in the loading tests are depicted in **Fig. 3.6**, taking specimen T-A at R=0.04 rad as an illustrative example. The visual representation clearly shows the conversion of frame displacement into the rotation of the upper member through the braces, and subsequently, into the torsion of the damper. Notably, even under substantial deformation at R=0.04, both the system and damper exhibited stable operation. This underscores the demonstrated compatibility of the proposed system with the frame.

Fig. 3.7 illustrates the correlation between the damper torsional angle and story drift angle as measured in the experiments, alongside the theoretical predictions using Eqs. (2.16) and (2.17) for the three specimens. The horizontal axis represents the story drift angle denoted as R, while the

vertical axis represents the damper torsional angle represented by θ. The amplification factors (θ/R) within the elastic range, calculated using Eq. (2.16) for specimens T-A, T-B, and T-C, are 2.96, 2.66, and 2.77, respectively. In the plastic range, the amplification factor (θ/R) is consistently 3.21 for all specimens as determined by Eq. (2.17). **Fig. 3.7** visually demonstrates that the damper torsional angle θ follows the boundaries provided by Eqs. (2.16) and (2.17), showcasing the validity of the theoretical predictions.

In **Fig. 3.8**, the relationship between brace axial force and story drift angle is presented. The labels L and R correspond to the bracing members connected to the left and right sides of the upper member, as indicated in **Fig. 3.1**. The findings illustrate that the brace axial force remains in a tensile state throughout the loading process, suggesting minimal deformation in the braces. When the story drift angle reaches 0.01 rad, resulting in an approximate lateral displacement of 15 mm for the frame, the axial deformation of a brace with a 42° inclination could potentially exceed 10 mm if the upper member does not rotate. This magnitude is notably larger than the yield deformation. Consequently, the rotation of the upper member is deemed fundamentally crucial for the operational dynamics of the seesaw-twisting system.

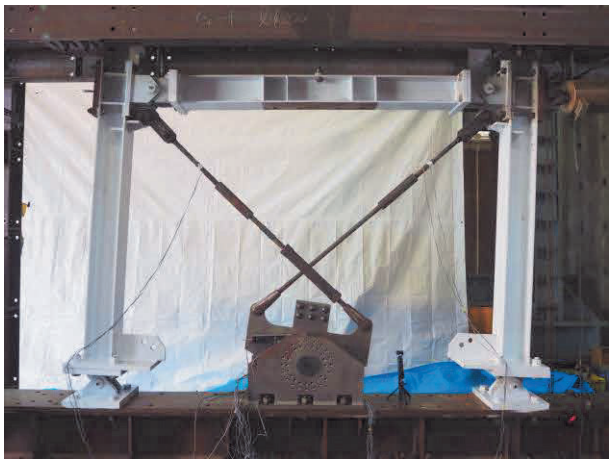

(a)

(b)

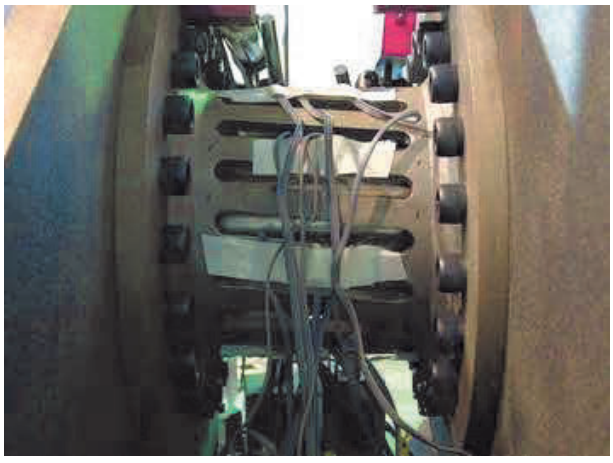

(c)

Fig. 3.6. Deformation of test specimen T-A at R= 0.04 rad:
(a) overall view; (b) damping device; (c) damper.

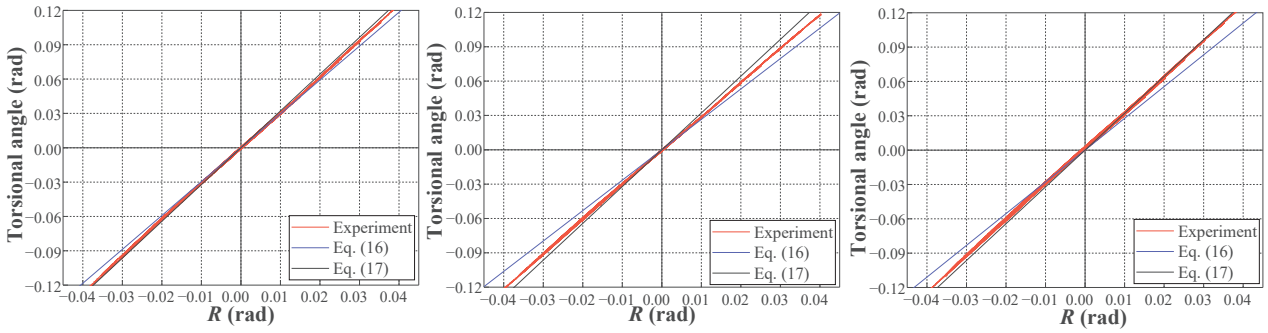

(a)Specimen T-A (b) Specimen T-B (c) Specimen T-C

Fig. 3.7. Damper torsional angle and story drift angle relationships.

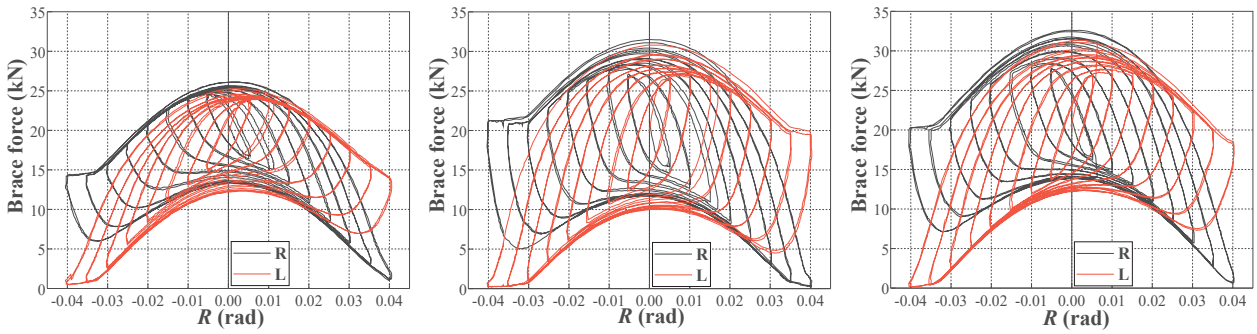

(a)Specimen T-A (b) Specimen T-B (c) Specimen T-C

Fig. 3.8. Brace axial force and story drift angle relationships.

3.6.3 Strip behavior

Fig. 3.9 depicts the strain measured during the initial loading stage of specimen T-B, categorized into tension, compression, and middle positions. The vertical axis represents the normalized lateral force, while the horizontal axis represents the normalized strain. As detailed in Section 2.2.1, in the torsional state of the CSSD, an anticipated bending of the strips was expected with an inflection point at the midpoint (refer to **Fig. 2.3**(c)). As the loading test for specimen T-B commenced, strain values at positions T-2, T-3, B-2, B-3, L-2, L-3, R-2, and R-3 increased on the tension side, while those at positions T-1, T-4, B-1, B-4, L-1, L-4, R-1, and R-4 increased on the compression side. All measured strips initially exhibited similar elastic deformation, transitioning into plasticity when the normalized lateral load reached 1. This observation validates the plastic mechanism analysis. Consequently, it is evident that the torque moment is uniformly converted to the tangential force of each strip in the CSSD. Strains at the tension and compression positions demonstrate almost symmetrical behavior, while those at the middle position remain limited. This suggests that the strip deformation closely aligns with anti-symmetrical flexural deformation in double curvature, without significant axial deformation.

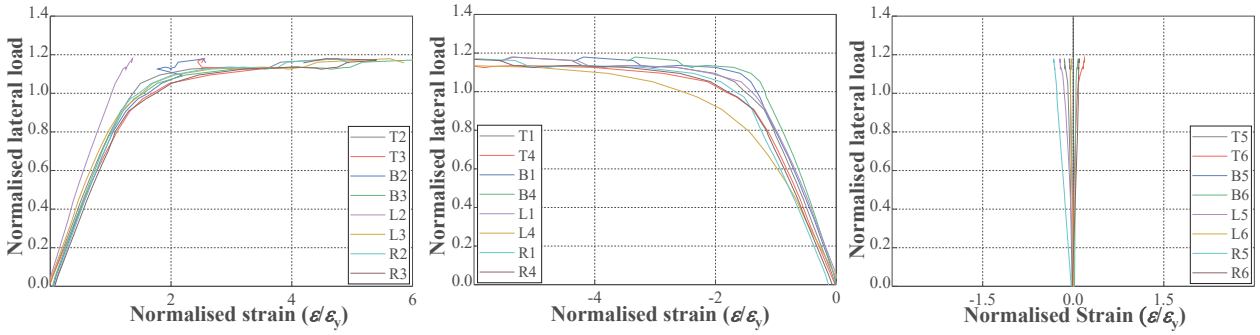

(a) Tension side (b) Compression side (c) Middle position

Fig. 3.9. Axial strain measured on strips of Specimen T-B.

3.6.4 Cumulative plastic deformation capacity and failure form

In the case of specimen T-A-c, subjected to a constant story drift angle of 0.03 rad, substantial strength reduction did not manifest until the latter half of the 67th loading cycle. The story drift angle of 0.03 rad is a deformation that rarely occurs even in actual rare seismic events. Therefore, 67 cycles are considered a significant number of loading cycles. The experimental procedure persisted with audible clacks indicating metal fractures until the load gradually diminished to half of its initial value, spanning a total of 84 loading cycles. Notably, all fractures occurred exclusively at the roots of the strips, as depicted in **Fig. 3.10**. Of particular value and significance is the observation that the system did not experience immediate failure following the decline in strength. Instead, the strength exhibited a gradual step-by-step reduction. Even after clear strength reduction in the latter half of the 67th loading cycle, this lightweight specimen (approximately 11.5 kg) demonstrated an impressive capability to dissipate 100.6 kJ of energy. Subsequently, without an abrupt and complete failure, it continued to absorb an additional 18.5 kJ of energy until the strength decreased to half of its maximum. This underscores the system's remarkable stability and substantial capacity for energy dissipation.

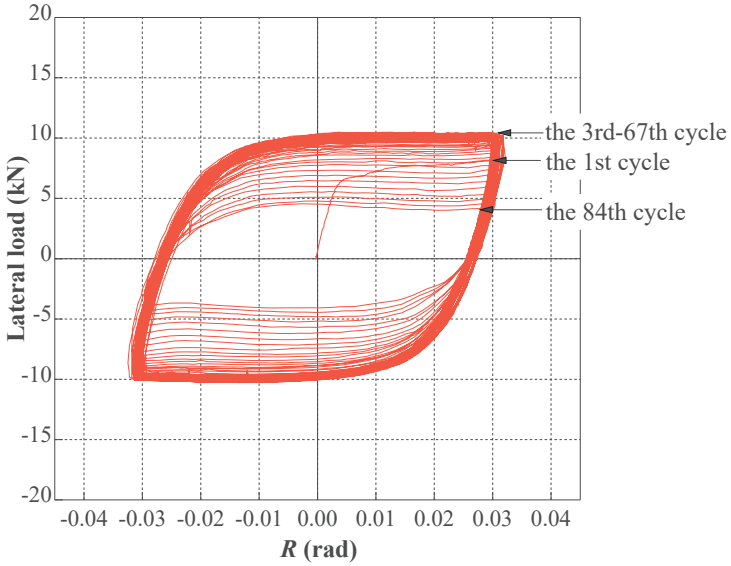

Fig. 3.10. Lateral load and story drift angle relationship of specimen T-A-c.

To quantify the plastic deformation capacity of the proposed damper, we introduce the cumulative plastic deformation ratio η. This ratio is defined as follows to encapsulate the plastic deformation ability:

$$\eta = \frac{|{}_{\mathrm{cum}}\delta_{\mathrm{p}}^{+}| + |{}_{\mathrm{cum}}\delta_{\mathrm{p}}^{-}|}{\delta_{\mathrm{y}}} \tag{3.1}$$

where ${}_{\mathrm{cum}}\delta_{\mathrm{p}}^{+}$ and ${}_{\mathrm{cum}}\delta_{\mathrm{p}}^{-}$ represent the cumulative plastic deformation in the positive and negative loading directions, respectively. These values can be extracted by delineating the curve of the load-displacement relationship illustrated in **Fig. 3.11** [30]. δ_{y} signifies the lateral yield deformation of the frame, determined by dividing $F_{\mathrm{y}}^{\mathrm{eval}}$ by k_{eval}, as derived from Eqs. (2.12) and (2.11), respectively. The recorded η value for specimen T-A-c stood at 3453 before any noticeable strength reduction occurred, underscoring the robust deformation capacity of the twisting system incorporating the CSSD. After strength deterioration, the bearing capacity of the system decreased gradually with each loading cycle rather than sudden failure.

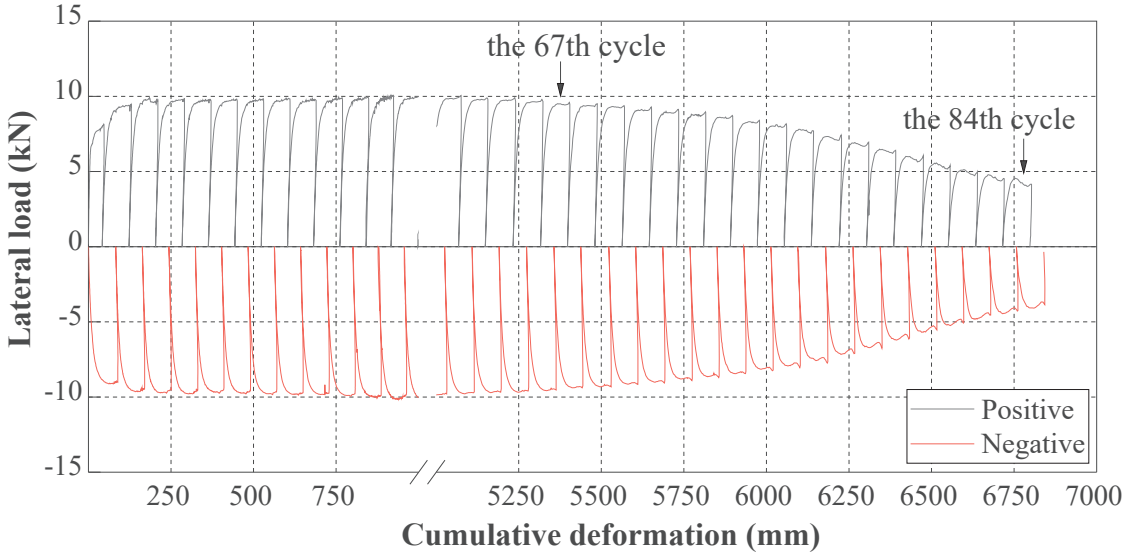

Fig. 3.11. Lateral load and cumulative deformation relationship of specimen T-A-c.

The failure modes of specimen T-A-c are illustrated in **Fig. 3.12**. In this particular specimen featuring 18 strips, penetrating fractures were observed at the ends of 14 strips, while cracks were noticed at the edges of the remaining 4 strips. Examining the flatter fatigue fracture in the 67th cycle (as depicted in **Fig. 3.12**(a)), the fracture surface reveals two distinctive regions: one comprises a smooth fatigue crack development zone with clearly defined shell pattern streaks, while the other displays a rough final rupture zone. The shell pattern lines are fully developed and exhibit wavy progression. In contrast, the strength failure fracture observed in the 84th cycle (as shown in **Fig. 3.12**(b)) follows a tortuous path, and the fracture surface exhibits coarse granular characteristics.

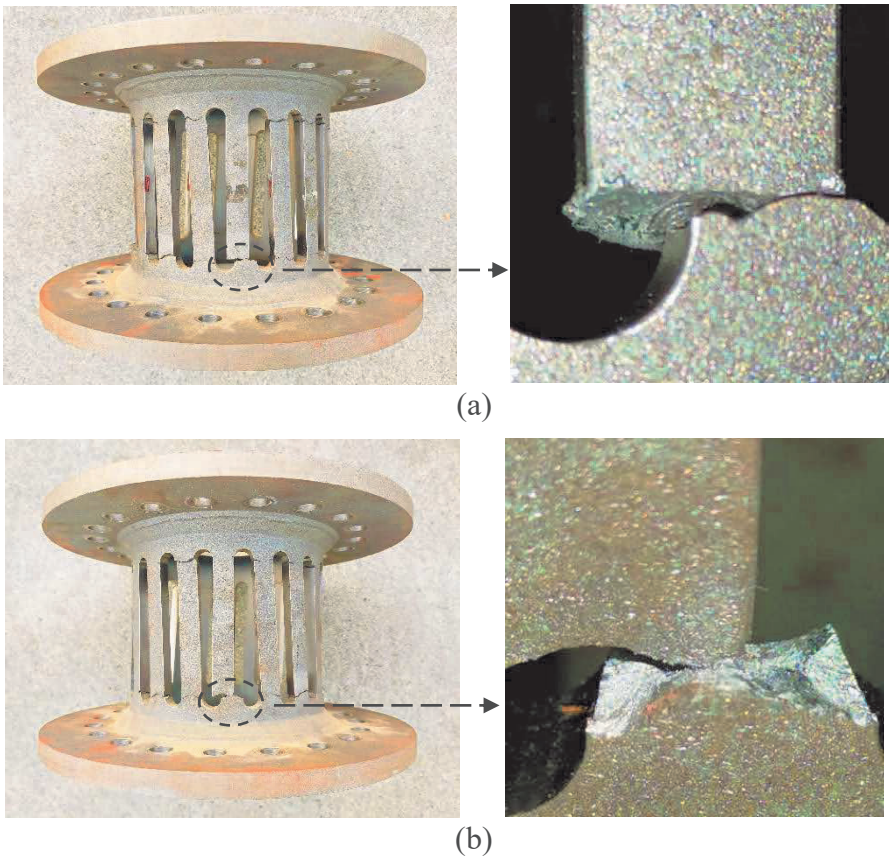

Fig. 3.12. Failure form of test specimen T-A-c: (a) fatigue failure fracture of the 67th cycle; (b) strength failure fracture of the 84th cycle.

3.6.5 Bi-linear hysteretic model

An abbreviated hysteretic model of the damping system is imperative for structural design, which necessitates precise quantitative calculations. To simplify the representation of the proposed energy dissipation system's experimental curves, a concise bi-linear model, depicted in **Fig. 3.13**, is employed. This model utilizes straight lines to simplify the complexities observed in the experimental data. Given that a story drift angle of 0.02 rad is commonly utilized as the story drift limit in the design of building structures, the determination of the bi-linear model is based on the test results of specimens T-A, T-B, and T-C up to R=0.02 rad, with no observed strength degradation. The model incorporates four parameters, where the elastic stiffness K_1 corresponds to the lateral system stiffness k_{eval}, derived from Eq. (2.11). The lateral system stiffness k_{eval} is calculated using the torsional stiffness of the CSSD S_D, obtained from Eq. (2.2), in which the stiffness reduction factors c for specimens T-A, T-B, and T-C are determined to be 0.78, 0.76, and 0.73, respectively, based on the torque moment and torsional angle of the CSSD obtained from the tests. P_y represents the initial lateral yield strength,

calculated as the sum of F_y^{eval} (obtained from Eq. (2.12)) and the frictional resistance (1.2 kN). The values of k_{eval} and F_y^{eval} for the three specimens are detailed in **Tables 2** and **3**, respectively.

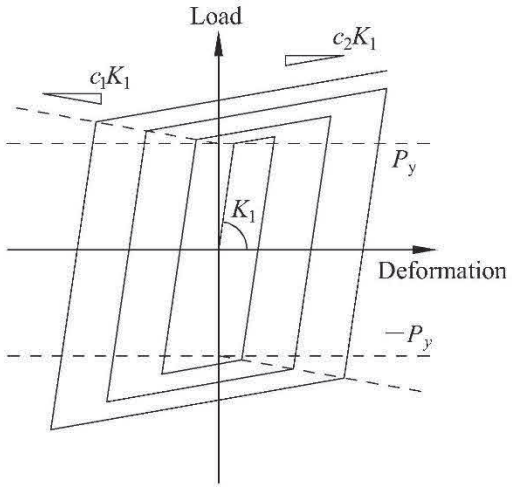

Fig. 3.13. Bi-linear hysteretic model.

Additionally, the enhancement ratios of strength relative to isotropic and kinematic hardening, denoted as c_1 and c_2, respectively, were established based on test results. These values were determined by assessing the similarity of hysteretic curves and the precision of energy dissipation fitting. The accuracy of fitting was evaluated by examining the disparities in energy dissipation between the test outcomes and the bi-linear model. Two metrics, E_{total} and E_{sum}, were employed to measure the energy dissipation difference. E_{total} represents the absolute disparity in total energy dissipation, while E_{sum} is the sum of absolute differences at amplitude points. In accordance with the concordance with hysteretic curves and the minimization of energy differences, detailed in **Appendix A**, the values selected for c_1 were 0.23, 0.11, and 0.14 for specimens T-A, T-B, and T-C, respectively. Additionally, c_2 was determined as 0.01 for all three specimens. From the computational process, it was found that, compared to kinematic hardening ratio c_2, isotropic hardening ratio c_1 plays a more significant role for the proposed CSSD.

The comparison of the hysteretic curve and energy dissipation between the test results and the bi-linear model, up to R=0.02 rad, is illustrated in **Fig. 3.14**. The left-side graphs initially demonstrate a fundamental concurrence between the bi-linear model and the test curve, encompassing both pattern and value levels. Subsequently, the right-side graphs depict a near-perfect alignment between the energy dissipation curves of the bi-linear model and the experimental results. Notably, the differences in total dissipated energy are consistently below 1.0%. This concise analysis model effectively quantifies the cyclic behavior of the damping system.

The variance in the most appropriate c_1 values for the three specimens can be attributed to the disparity in their respective yield story drifts. This distinction is evident in **Table 4**, where the yield

story drift angles follow an ascending order of T-B, T-C, and T-A. Under identical loading programs, the severity of yield and the inclination of the yield curve exhibit a progression from severe to mild and from gentle to steep, respectively. Consequently, the optimal c_1 values are determined as 0.11 (T-B), 0.14 (T-C), and 0.23 (T-A).

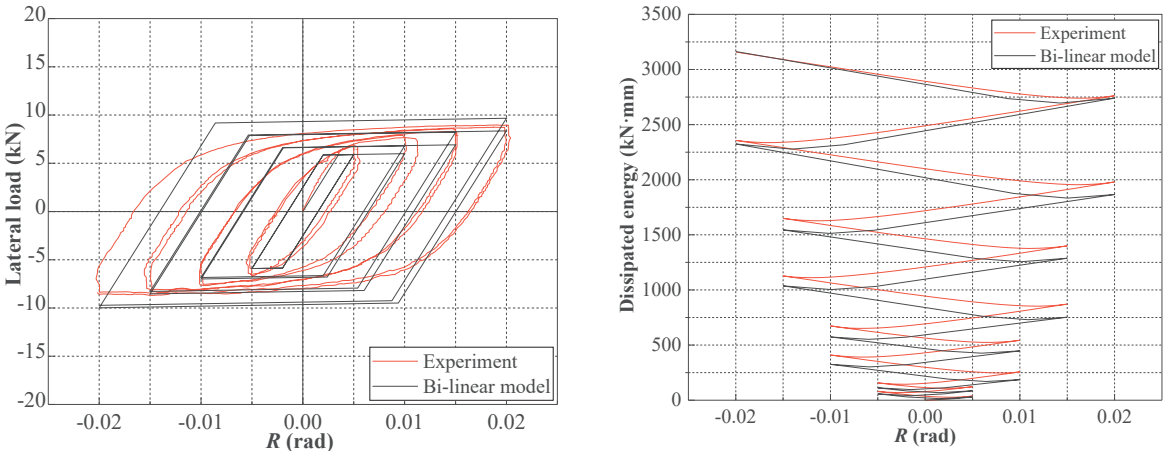

(a) Specimen T-A

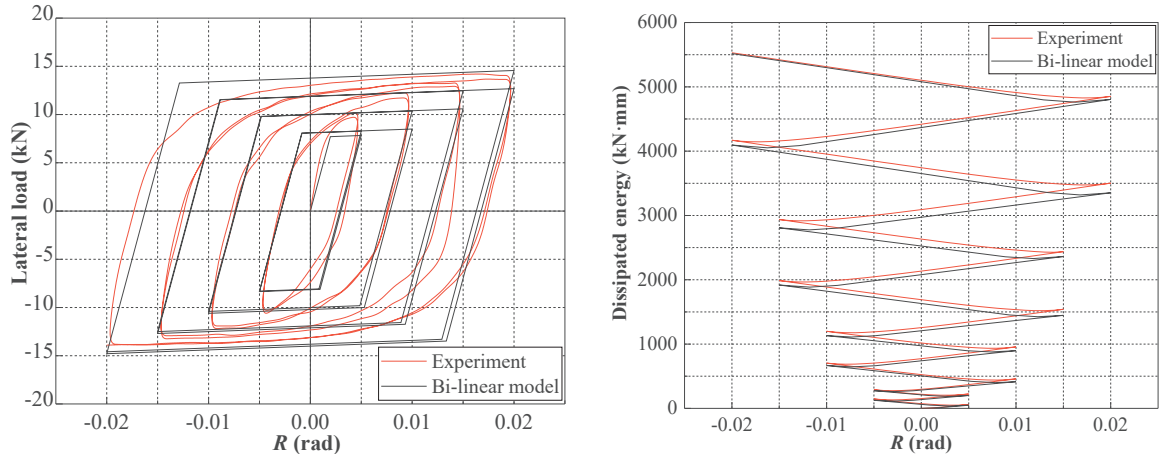

(b) Specimen T-B

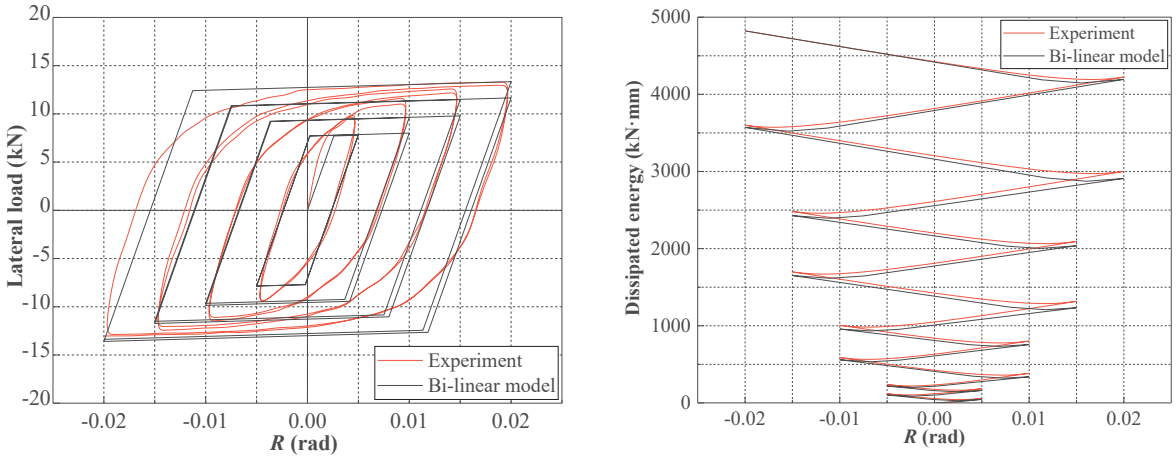

(c) Specimen T-C

Fig. 3.14. Comparison of hysteretic model with test results.

4. NUMERICAL STUDY FOR THE CSSD

4.1 General

To investigate the detailed stress distribution of the proposed CSSD, finite element analysis (FEA) was conducted for the three dampers. Hysteresis loading and one-directional one-way loading analyses, provided by ANSYS 2019 R1, were utilized in our numerical simulations. The analysis results exhibit good agreement with the laboratory testing results in the hysteresis curves and one-directional loading curve, as shown in **Fig. 4.2** to **Fig. 4.3**. The FEA reveals a uniform distribution of torque load across all strips, with stress concentration notably observed at the root of the strips. This observation aligns consistently with the locations where cracks formed during the experimental phase. Additionally, comprehensive details regarding the FEA parameters and results are presented in the subsequent sections.

4.2 Analysis models and setting

For this investigation, the simulation software employed was ANSYS 2019 R1. The analysis model corresponding to the test specimen T-A is visually represented in **Fig. 4.1**. Notably, the models did not take into account the specific details of welded and bolted connections. The modeling of the end plates and CSSD was achieved using the multi-layered eight-node shell element 281 in ANSYS.

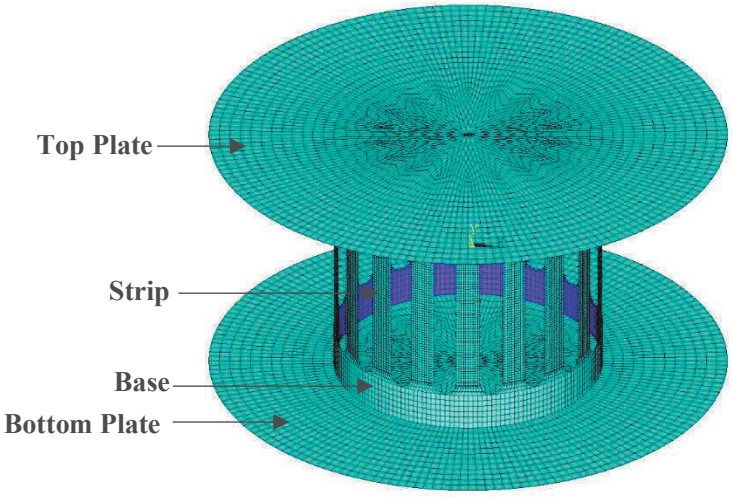

Fig. 4.1. FE model of the specimen T-A.

Complete constraints were imposed on all degrees of freedom of the nodes along the bottom plate edge. Concurrently, forced displacements were applied to the nodes positioned along the edge of the top plate.

4.3 Steel materials

The damper material's yield and ultimate stresses were assigned based on the outcomes of the tensile coupon tests, as detailed in Section 3.3. Young's modulus was specified as 2.05×10^5 N/mm², while Poisson's ratio was set at 0.3. The plastic properties of the damper material adhered to the Von Mises yield criterion, incorporating isotropic-kinematic hardening effects. In this analysis, the isotropic hardening ratio was established at 0.005, and the Chaboche kinematic hardening parameters were configured with C=1025 N/mm² and γ=256. The hardening ratio parameters are derived from tensile coupon tests. The definitions of C and γ can be found in Ref. [36].

4.4 Loading programs

As previously described, all the degrees of freedom of the nodes along the bottom plate edge were fully constrained. In parallel, forced displacements were administered to the nodes located along the top plate edge. The numerical investigation encompassed both hysteresis loading and one-directional one-way loading analyses.

In the specific context of hysteresis loading, it is noteworthy that the torsional amplitude of the CSSD for each loading cycle precisely matched the loading amplitude employed in the experimental configuration. This meticulous alignment ensured that the numerical simulations faithfully replicated the experimental conditions, allowing for a comprehensive and accurate analysis of the CSSD performance under hysteresis loading condition.

4.5 Analysis results

4.5.1 Experimental and numerical hysteresis curves

Fig. 4.2 illustrates a side-by-side evaluation of hysteresis curves obtained from experimental data and FE analyses. The torsional angle and torque moment of the CSSD are represented on the horizontal and vertical axes, respectively. The torque moment in the experimental dataset was computed utilizing the axial force measurements of the two braces recorded during the experiment. The graphical representation in **Fig. 4.2** serves as a visual comparison between the hysteresis curves derived from experimental observations and those generated through FEA. Notably, the analysis results exhibit hysteretic behavior that closely aligns with the experimental data discussed in the preceding section.

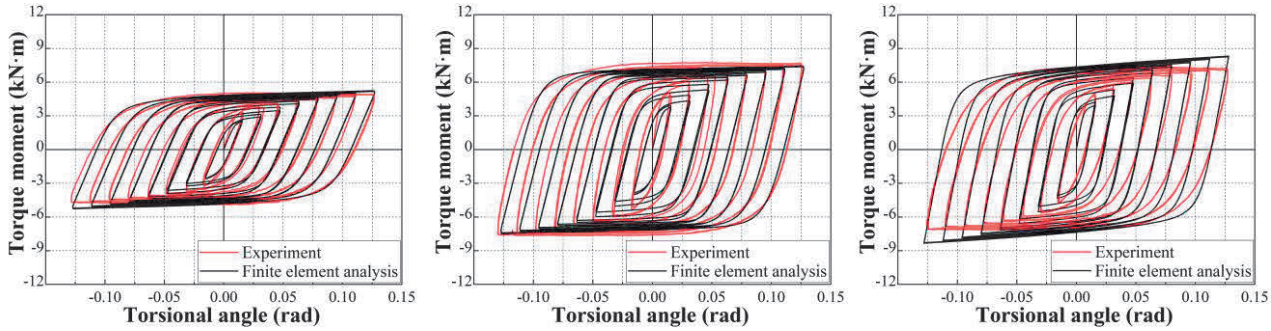

(a) Specimen T-A (b) Specimen T-B (c) Specimen T-C

Fig. 4.2. Comparison of experimental and numerical hysteresis curves.

4.5.2 Experimental skeleton and numerical monotonic curves

In **Fig. 4.3**, a comparison of the experimental skeleton curves and monotonic FE analysis is depicted. The curves generated through FEA exhibit a comparable prediction of the observed tendencies in the test skeleton curve, with yielding occurring at nearly the same damper rotation angle. Particularly for specimen T-A, the FEA curve closely aligns with the experimental counterpart. However, for specimens T-B and T-C, the FEA results indicate slightly lower values compared to the experimental data. This discrepancy can be attributed to the inherent frictional resistance within the system.

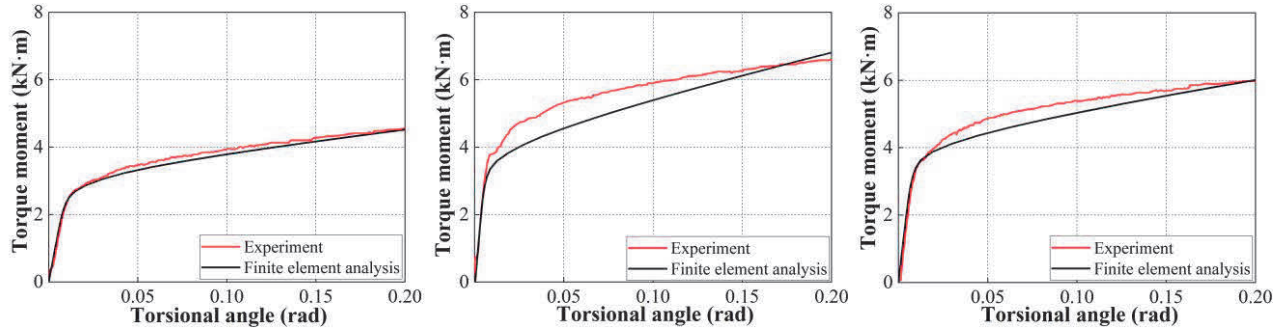

(a) Specimen T-A (b) Specimen T-B (c) Specimen T-C

Fig. 4.3. Comparison of skeleton curves with numerical monotonic analysis.

4.5.3 Stress distribution

In **Fig. 4.4**, the distribution of equivalent von Mises stress in the FEA model is presented at a torsional angle of 0.01 rad applied to the CSSD. The yield regions, depicted in red, indicate that all models of the three specimens experienced yielding. Notably, all three specifications exhibit similar stress characteristics. The torque load is evenly distributed among all strips, resulting in stress concentration at the root of the strips, a pattern consistent with the locations where cracks formed during the experimental phase. Along the strip, stress rapidly diminishes outside the root, and the stress in the base part is notably minimal.

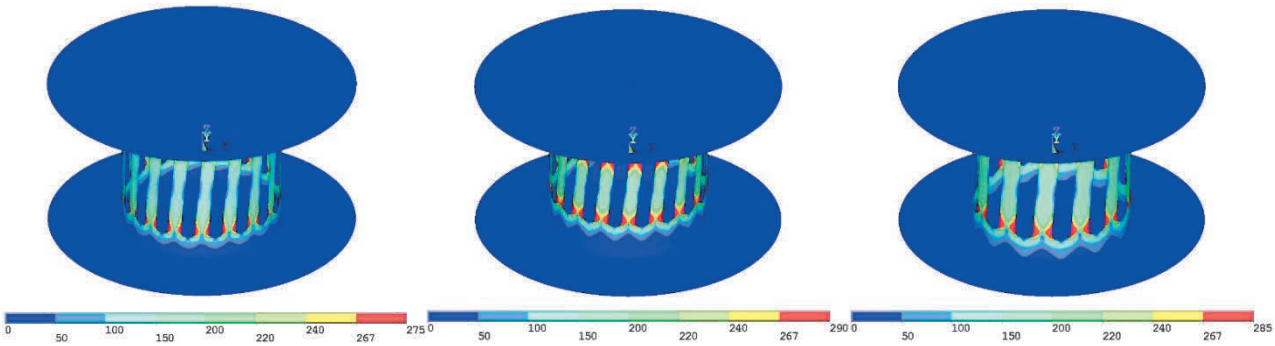

(a) (b) (c)

Fig. 4.4. Von-Mises stress for θ=0.01 rad: (a) specimen T-A; (b) specimen T-B; (c) specimen T-C.

4.5.4 Initial lateral stiffness, lateral yield strength, and yield story drift angle

Tables 2, **3**, and **4** present the initial lateral stiffness, lateral yield strength, and yield story drift angle, respectively, determined through a comprehensive analysis involving theoretical evaluation, FEA, and experimental tests. The ratios of the initial lateral stiffness and lateral yield strength from theoretical and FEA assessments to the corresponding experimental values are also provided. The predicted initial lateral stiffness (k_{eval}) and lateral yield strength ($F_{\text{y}}^{\text{eval}}$) were derived using Eqs. (2.11) and (2.12), respectively. The lateral yield strength from FEA ($F_{\text{y}}^{\text{FEA}}$) and tests ($F_{\text{y}}^{\text{test}}$) were defined as the lateral load at which the lateral stiffness decreased to one-third of the initial value. The lateral system stiffness and load from FEA were determined based on the relationship between the frame and damper, as expressed in Eqs. (2.5), (2.9), and (2.12). The yield story drift angles were calculated as the lateral displacement divided by the frame height of 1568 mm at the yield point. Comparisons between theoretical evaluations, FEA results, and experimental measurements demonstrate satisfactory correspondence for the initial lateral stiffness, lateral yield strength, and yield story drift angle. Notably, all dampers exhibit plastic deformation at a small story drift, indicating an early triggering of damper yielding for effective energy dissipation during seismic events. Additionally, the system characteristics exhibit a specific variation range due to differences in damper geometry, allowing for the design of a relatively broad spectrum of structural properties. For instance, specimens T-B and T-C have the same lateral strengths in the evaluation, but differing initial stiffness, highlighting the independent design possibilities for the lateral strength and initial stiffness of the proposed system.

Table 2 – Initial lateral stiffness (units: kN/mm)

	k_{eval}	k_{FEA}	k_{test}	k_{eval}/k_{test}	k_{FEA}/k_{test}
T-A	1.16	1.10	1.28	0.90	0.86
T-B	2.55	2.21	2.88	0.89	0.77
T-C	2.02	1.70	2.12	0.95	0.80

Table 3 – Lateral yield strength (units: kN)

	F_y^{eval}	F_y^{FEA}	F_y^{test}	F_y^{eval}/F_y^{test}	F_y^{FEA}/F_y^{test}
T-A	4.66	5.08	4.86	0.96	1.05
T-B	6.51	6.94	7.16	0.91	0.97
T-C	6.51	6.88	7.51	0.87	0.92

Table 4 – Yield story drift angle (units: rad)

	R_y^{eval}	R_y^{FEA}	R_y^{test}	R_y^{eval}/R_y^{test}	R_y^{FEA}/R_y^{test}
T-A	0.0026	0.0037	0.0035	0.73	1.06
T-B	0.0016	0.0025	0.0022	0.74	1.14
T-C	0.0021	0.0032	0.0030	0.69	1.07

5. SEISMIC PERFORMANCE OF STEEL STRUCTURES WITH STS USING CSSD

5.1 General

Following the performance study of the STS with CSSD, this section inquired into the seismic performance of an STS utilizing a three-story steel moment frame as a prototype structure. The seismic response analyses, centering on a standard STS configuration, were initially conducted. The peak inter story drift angles were examined under variations in the beam section, system stiffness and strength, and system specifications. An integral feature of an STS lies in its capacity to facilitate the utilization of extended steel rods for bracing between the seesaw member and frame connections across multiple stories. Consequently, additional frames with four distinct STS configurations were analyzed to examine the peak story drift angles and plastic hinge formation. The effect of the amplification factor on the seismic response of the frame with diverse configurations was discussed. The findings demonstrated the effective reduction of peak story drifts by the STS with the CSSD.

5.2 Prototype building and typical STS configuration

5.2.1 Design of prototype building and typical STS configuration

In **Fig. 5.**1, the schematic representations illustrate the analytical models of the prototype building and the typical damping system configuration. A bare steel moment frame (BF), designed as a prototype building, satisfies the current seismic code requirements of Japan for strength and drift. This three-story frame spans six meters per span and features fixed constraints at all column bases in the first story. The first story has a height of 4.5 m, while the second and third stories each have a height of 4 m. Square hollow sections of □-400×16 (□-width × thickness, unit: mm) are used for columns, and H-450×200×9×14 (H-depth × flange-width × web-thickness × flange-thickness, unit: mm) are used for beams. The assumed yield strength of the steel material is 235 N/mm^2. Plastic moments at the column and beam ends are assumed to be M_p = 832 kN·m and M_p = 387 kN·m, respectively. Each floor has a standardized mass of 60 t, with 10 t assigned to each edge beam-to-column connection (represented by smaller solid circles ● in Fig. 5.1) and 20 t assigned to each intermediate beam-to-column connection (represented by larger solid circles ⬤). Eigenvalue analysis results in a primary natural period of 0.682 seconds.

In Model A (MA), an STS damping system is incorporated at the midspan of each story, illustrated in **Fig. 5.1**. Model A stands out as the most straightforward to implement when compared to Models B–E, as depicted in **Fig. 5.19**, and represents a conventional arrangement. It integrates 90 mm diameter tension rods as bracing elements. The parameters employed in Model A, along with their

respective properties such as rod length and stiffness (k_B), angles α and β, distances w and e, amplification factor f_{st}^{p}, and fundamental natural period T, are detailed in **Table 5**.

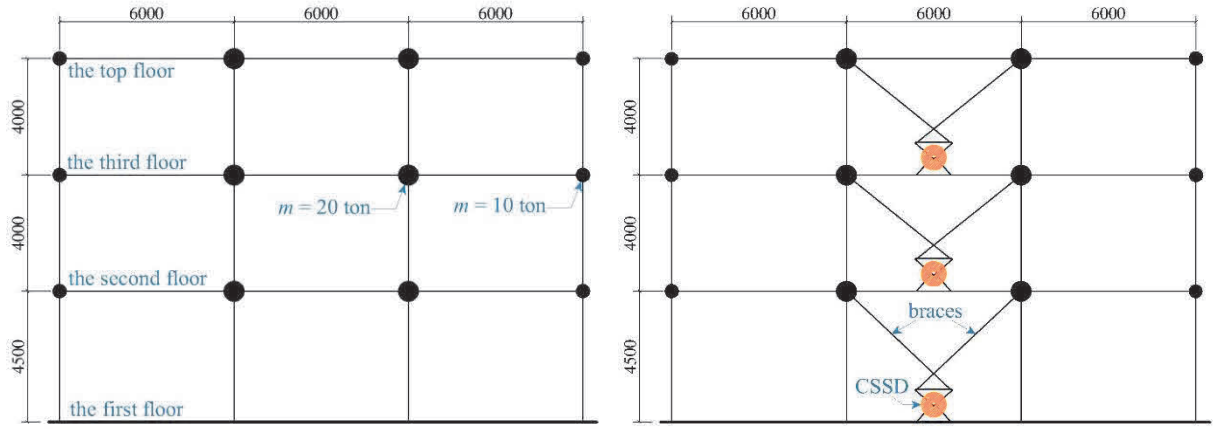

Model BF (BF) Model A (MA)

Fig. 5.1. Prototype building and typical damping system configuration.

Table 5 – Parameters and properties of the analysis models with various configurations

Model		ID	Steel rod brace length (mm)	Steel rod brace stiffness (kN/mm)	α (°)	β (°)	w (mm)	e (mm)	f_{st}^{p}	T (s)
Model BF		BF	—	—	—	—	—	—	—	0.682
Model A	1st floor	MA	4,952	263	43	40	600	775	4.24	0.566
	2nd, 3rd floor		4,623	282	39	40	600	766	3.77	
Model B		MB	14,904	87	50	40	600	781	10.27	0.446
Model C		MC	12,121	108	38	40	600	762	8.75	0.600
Model D		MD	11,955	109	72	40	600	723	5.33	0.614
Model E		ME	8,229	158	64	40	600	758	4.91	0.470

The damping system implemented in each story of Model A (MA) was configured to exhibit equivalent lateral stiffness to the corresponding story in the bare frame and 20% of its strength, as per Eqs. (2.11) and (2.12), respectively. The kinematic hardening ratio of the CSSD was set to 0.01, a value established in prior experimental investigations [38]. **Table 6** provides selected CSSD designs as illustrative examples, acknowledging that multiple designs can meet a design requirement. The presented CSSD design samples adhere to the common specifications of steel tube STKM13A, possessing a Young's modulus of 2.05×10^5 N/mm^2 and a Poisson's ratio of 0.3. A stiffness reduction factor of 0.6 was applied, drawing from insights obtained in previous experimental studies [37, 38]. Additionally, a consistent aspect ratio l'/b of approximately 5.5 was maintained for the strips throughout the design process. Notably, the table reveals a progressive reduction in the required diameter and thickness of the CSSD from the first to the third story.

Table 6 – Dimensions of selected CSSD designs

	σ_y (N/mm²)	D (mm)	t (mm)	l' (mm)	b (mm)	l'/b	n	c
1st story	325	426	45	137.8	26	5.3	32	0.6
2nd story	325	365	40	145.6	26	5.6	32	0.6
3rd story	325	355.6	35	112	20	5.6	32	0.6

In **Fig. 5.**2, the schematic details of the prototype damping device configuration are depicted. The CSSD is securely fastened at one end to the immovable bottom member, while the other end is attached to the upper member, enabling free rotation. The decision to avoid on-site welding during damper installation was driven by the imperative to mitigate construction uncertainties and simplify post-earthquake replacement procedures. Additionally, to ensure stable torsion and prevent warping, a supplementary support member was added parallel to the upper member.

The horizontal span between the two connection points is labeled as w_u, measuring 1200 mm, with its half, denoted as w, equating to 600 mm. The vertical distance from the connection point to the top surface of the beam is represented as h_{bc}, measuring 1100 mm. Within this span, the connection point is positioned at a distance of 500 mm from the rotational center (h_u), while the rotational center itself is situated 600 mm above the top surface of the beam, designated as h_b.

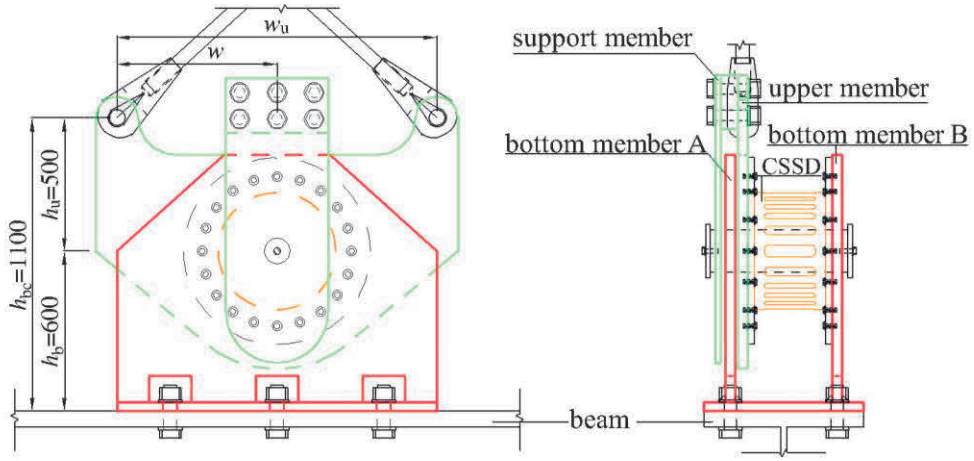

Fig. 5.2. Configuration of prototype damping device: (a) front elevation, (b) side elevation.

5.2.2 Description of analysis models

The seismic response analysis of both the bare frame and the steel structure equipped with the CSSD was conducted through the development of plane frame models using OpenSees [39]. **Fig. 5.3** illustrates the analytical model. To account accurately for the coupling between the axial force and the bending moment, as well as the spreading of plasticity within the structural elements, force-based beam–column elements and fiber sections were employed to model the beams and columns. A

uniaxial Steel01 material model was applied to the beams and columns, establishing a bilinear stress–strain relationship with a kinematic hardening rule. All the beam–column connections were rigid. Truss elements with elastic materials were employed to model the braces, simulating their behavior without introducing yielding or buckling issues. It's worth noting that pretension was deemed necessary for the diagonal rods in the STS damping system to ensure constant tension in the braces. However, for the dynamic analysis conducted in this study, elastic truss elements without pretension were utilized to model the braces. Despite the cyclic tension and compression experienced by the truss elements, differing from the behavior of rod braces in tension, the presented numerical analysis can faithfully replicate the dynamic response and accurately simulate the working conditions of the CSSD, aligning with the overall structural behavior.

The upper member, represented by the inverted triangle ABO in green, and the bottom member, denoted as triangle A'B'O' in red, were simulated using force-based beam–column elements with elastic sections. To closely approximate the actual behavior of the components with minimal deformation, an exceptionally high elastic modulus was assigned for upper and bottom members.

Notably, points O and O', although possessing identical coordinates, served as distinct points, enabling the use of zero-length elements to model the CSSD. The relative translation between these points was restricted, allowing only for relative rotation, thereby effectively replicating the real working conditions of the CSSD. To capture the torsional behavior of the CSSD, a rotational spring featuring initial torsional stiffness (S_{D}) and bearing torque ($T_{\mathrm{D}}^{\mathrm{P}}$) was introduced between points O and O'. The values of S_{D} and $T_{\mathrm{D}}^{\mathrm{P}}$ were computed using Eqs. (2.2) and (2.4), respectively. Additionally, the rigid diaphragm assumption was adopted to ensure uniform lateral displacements of the beam–column joints on each floor. All materials, sections, and elements utilized in this section can be referenced in the OpenSees user manual.

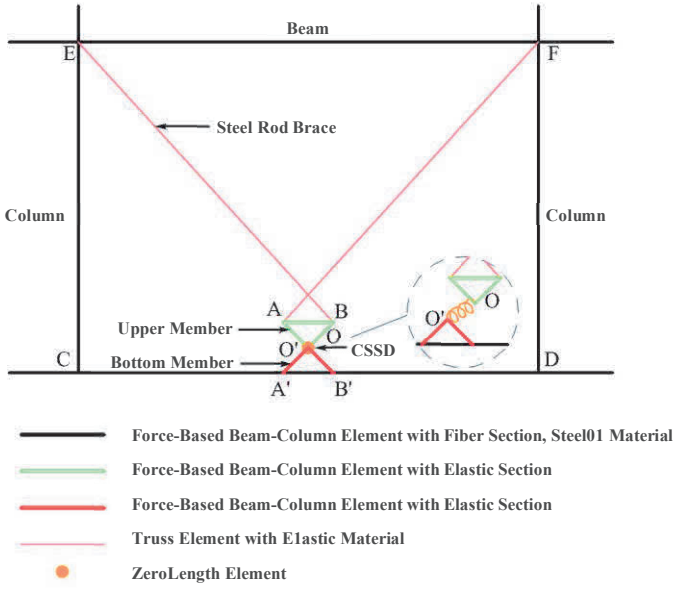

Fig. 5.3. Description of the analytical model.

5.2.3 CSSD element

In order to replicate the torsional characteristics of the CSSD, a rotational spring featuring initial torsional stiffness (S_D) and bearing torque (T_D^P) was introduced between points O and O'. The values for S_D and T_D^P were determined using the Eqs. (2.2) and (2.4), respectively. Additionally, to maintain uniform lateral displacements of the beam–column joints on each floor, the assumption of a rigid diaphragm was employed. All the details regarding the materials, sections, and elements utilized in this section are documented in the OpenSees user manual.

5.2.4 Input ground motions

The seismic response analysis incorporated four normalized recorded motions: El Centro NS (1940), Taft EW (1952), Hachinohe NS (1968), and JMA Kobe NS (1995), each featuring a seismic duration of 50 seconds. Two levels of ground motion intensity, denoted as Level 1 and Level 2, were considered in the analysis. To standardize the records, the four motions were scaled to achieve peak ground velocities (PGV) of 25 cm/s for Level 1 and 50 cm/s for Level 2. It is important to mention that PGV, a parameter frequently employed in Japan for scaling ground motion in building design, demonstrates a notably close correlation with structural damage. As per seismic design standards for high-rise buildings in Japan, Level 1 corresponds to strong earthquakes expected once or twice during a building's service life, while Level 2 represents the most severe earthquakes, featuring the highest magnitudes that could potentially occur in the future. For Level 2, the safety criterion necessitates the implementation of measures to prevent excessively large deformations, even if certain sections of the structure may enter the plastic range. **Table 7** outlines the nomenclatures of the input motions, along

with their corresponding scale factor, peak ground velocity (PGV), and peak ground acceleration (PGA).

Table 7 – Basic information on input ground motions (units: PGV, cm/s; PGA, cm/s^2)

Input motion	Nomenclature	Original waves		Normalized Level 1			Normalized Level 2		
		PGV	PGA	scale factor	PGV	PGA	scale factor	PGV	PGA
El Centro NS	el	33.5	341.7	0.75	25	255.4	1.49	50	510.8
Hachinohe NS	hachi	34.1	229.7	0.73	25	168.4	1.47	50	336.8
JMA Kobe NS	kobe	90.9	818.0	0.28	25	225.0	0.55	50	450.0
TAFT EW	taft	17.7	175.9	1.41	25	248.4	2.82	50	496.8

5.3 Seismic analysis of the typical STS configuration

5.3.1 Time-history responses of displacement

Fig. 5.4 and **5.5** illustrate the time-history responses of the top-floor displacement (u_t) for both the BF and MA under PGV conditions of 25 and 50 cm/s, respectively. The points corresponding to the maximum displacement are emphasized and annotated with their respective values. As depicted in the figures, the incorporation of dampers in the MA configuration resulted in a notable reduction in structural response to seismic loads. The maximum displacement at the top floor of the MA configuration exhibited a significant decrease compared to that of the BF.

Figs. 5.20 and **5.21** display the distributions of maximum story drift angles in the BF and MA, subjected to four earthquake motions with PGV values of 25 and 50 cm/s. The integration of the STS into the MA configuration resulted in a consistent reduction in inter-story drift across all cases, with minimal impact on the vibration mode. Specifically, for earthquake motions featuring a PGV of 50 cm/s, except for the El Centro earthquake, the maximum story drift angles in the MA were consistently below 0.01 rad. In **Fig. 5.6**, the hysteresis curves of the rotational spring simulating the CSSDs in the MA under the El Centro earthquake motion with a PGV of 50 cm/s are presented. The CSSDs of each story in the MA functioned properly. Notably, in the MA, the maximum torsional angle of the CSSDs followed a decreasing order across the second, first, and third stories, aligning with the observed inter-story drift angles.

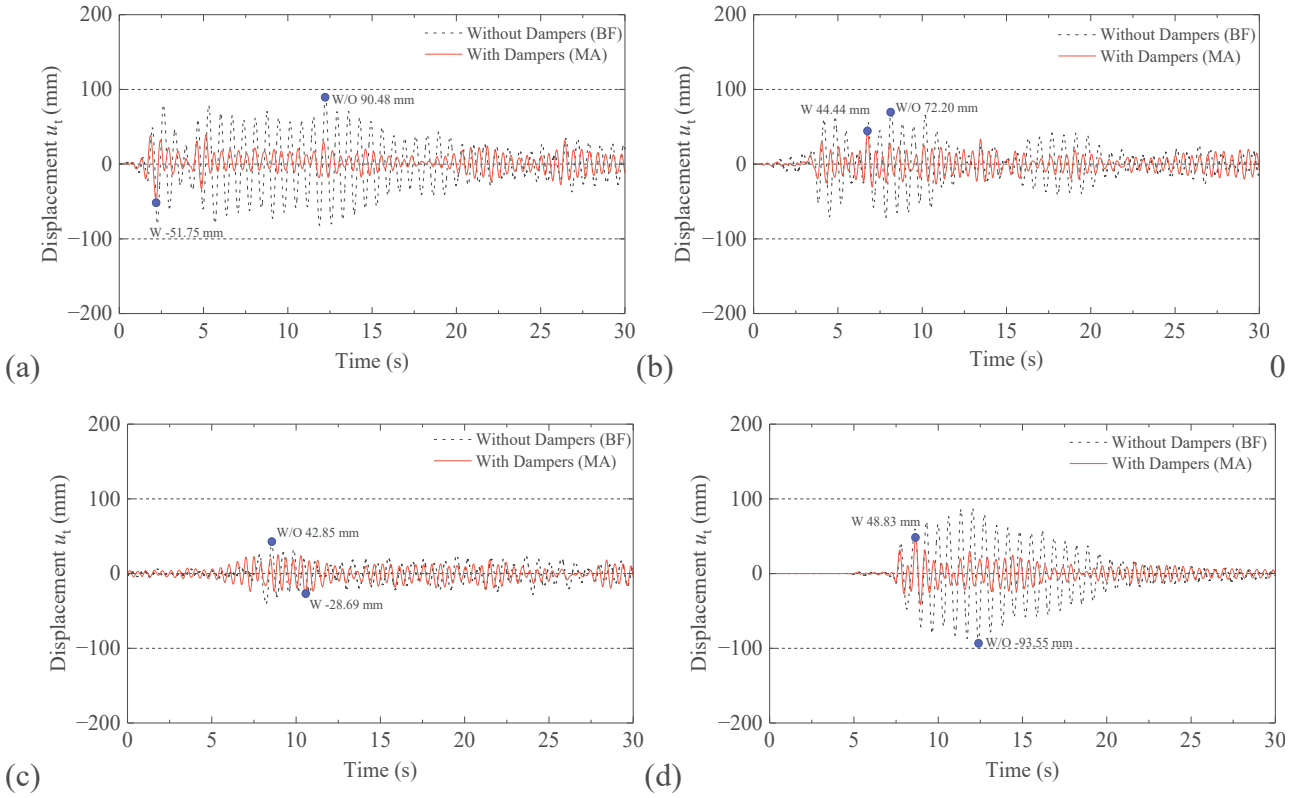

Fig. 5.4. Time-history response of displacement at the top floor of the BF and MA for ground motions with PGV = 25 cm/s: (a) el, (b) taft, (c) hachi, and (d) kobe.

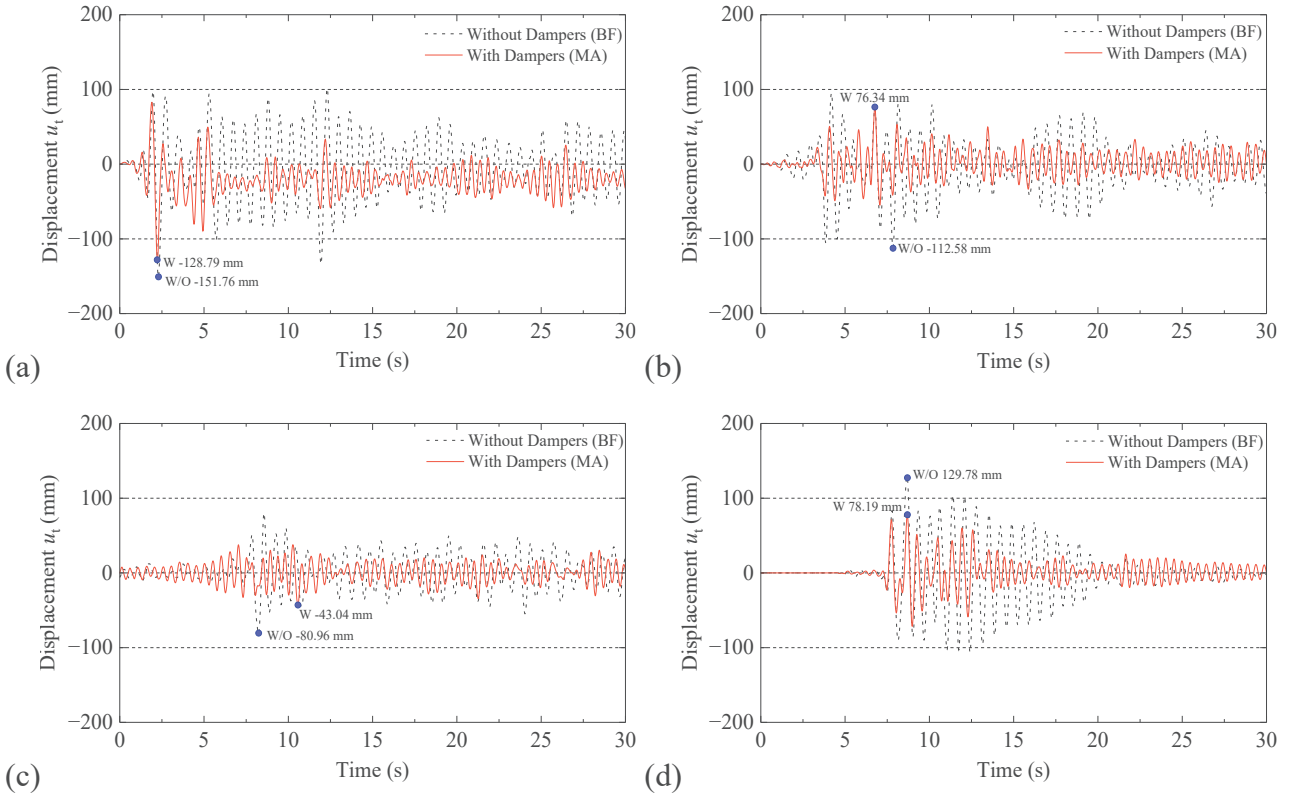

Fig. 5.5. Time-history response of displacement at the top floor of the BF and MA for ground motions with PGV= 50 cm/s: (a) el, (b) taft, (c) hachi, and (d) kobe.

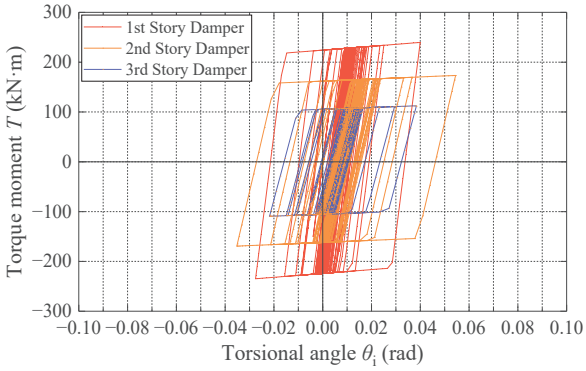

Fig. 5.6. Hysteretic curves of the CSSD in MA with PGV = 50 cm/s.

5.3.2 Influence of beam section dimension

Fig. 5.7 illustrates the maximum moment diagrams for the beams on the second and third floors in both the BF and MA, subjected to JMA Kobe with a PGV of 50 cm/s. Instances where the bending moment surpasses the yield bending moment of the beam end are highlighted by red numbers in the figure. Notably, in comparison to the BF, there is a noteworthy reduction in the bending moment at the beam end in the MA. This reduction can be attributed to the presence of STSs, which mitigate the maximum lateral displacement of the structure. Importantly, the sections of the beams connected to the bottom member did not yield, indicating that the beams effectively supported the operation of the dampers.

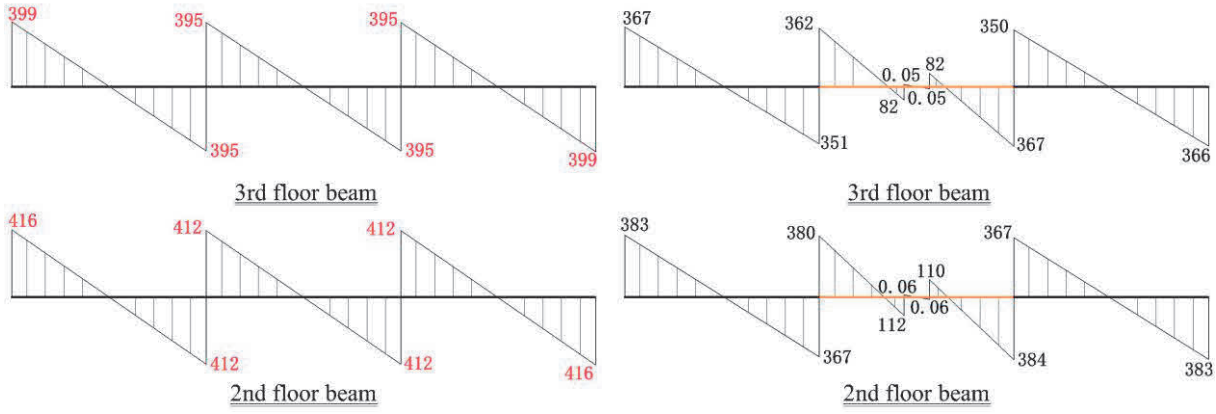

Fig. 5.7. Maximum moment diagrams of second- and third-floor beams for kobe with PGV = 50 cm/s: (a) BF, (b) MA.

To inquire deeper into the impact of beam cross-sections, the seismic responses of a structure equipped with dampers on beams featuring different cross-sections were investigated. In **Fig. 5.8**, the two beams highlighted in red were simultaneously replaced, while the remaining beam sections remained unchanged. The replaced sections adopted standard H-shaped steel profiles with section

heights ranging from 300 to 500 mm; the baseline model utilized a section height of 450 mm. **Fig. 5.8** provides the nomenclature, specific dimensions, and principal moments of inertia for the replaced beam sections. As outlined in Section 5.2.1, the stiffness of the STS for each floor was designed to match that of the corresponding floor in the BF, and its strength was set at 20% of that in the BF.

Fig. 5.9 depicts the maximum inter-story drift angles observed under four distinct seismic waves, with dashed lines representing the maximum inter-story drift angle of the BF. In all instances, a consistent decrease in the maximum inter-story drift angle, compared to that of the BF, was observed, regardless of the size of the beam section. For the El Centro and Hachinohe earthquake motions, an increase in beam height resulted in a gradual reduction in inter-story drift angles. Conversely, during the Taft and Kobe earthquake motions, there was an increase in the maximum inter-story drift angles, albeit with certain setbacks. This demonstrates the overall effectiveness of the dampers across all analyzed beam sections. Interestingly, when it comes to beam sections, a mere increase in the size of the beam section does not necessarily guarantee a reduction in the maximum inter-story drift angles. The effectiveness varies depending on the characteristics of the seismic waves.

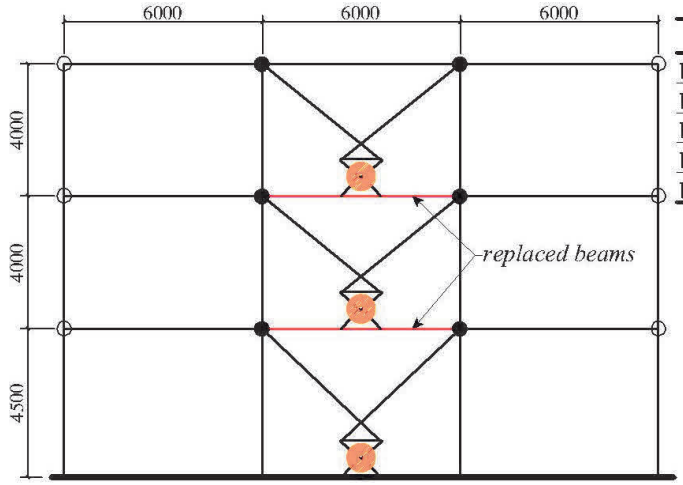

	Section $H\times B\times t_1\times t_2$ (mm)	I_x (mm^4)
bh300	H-300×150×5.5×8	6,320×10^4
bh350	H-350×175×6×9	11,000×10^4
bh400	H-400×200×7×11	19,800×10^4
bh450	H-450×200×9×14	32,900×10^4 *(baseline model)*
bh500	H-500×200×10×16	46,800×10^4

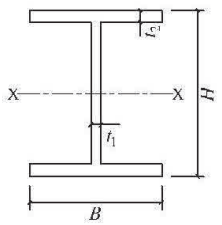

Fig. 5.8. Replaced beams and their cross-sections in the MA.

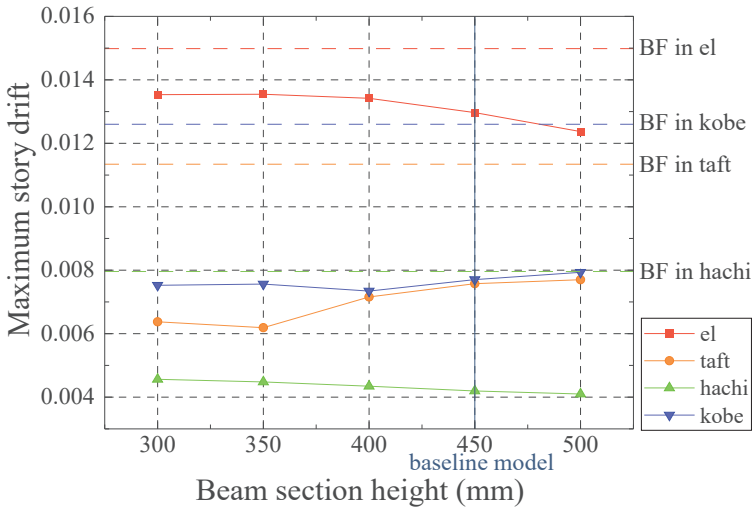

Fig. 5.9. Peak story drift angle of the MA with variation in the beam section for ground motion with PGV = 50 cm/s.

5.3.3 Influence of STS stiffness and strength

Figs. 5.10–5.13 depict the peak story drift (R_{peak}) of each story in the MA under four distinct earthquake motions, comparing it with the prototype bare frame. The STS stiffness ratios ranged from 0 to 400%, and the STS strength ratios increased from 0 to 50% relative to the bare frame. Notably, a stiffness ratio of zero or a strength ratio of zero signify that the frame is identical to the BF.

In all the graphs presented in **Figs. 5.10–5.13**, there is an overall decrease in the R_{peak} of each story as the stiffness and strength of the STS increase. However, it is noteworthy that when either the stiffness or strength is particularly low, a simple increase in either parameter individually has limited effect on reducing the R_{peak} value. Across all the earthquake motions examined, R_{peak} exhibited a rapid decrease when the stiffness ratio increased from 0 to 100%, and the strength ratio increased from 0 to 20%. Subsequently, the decreasing trend slowed down.

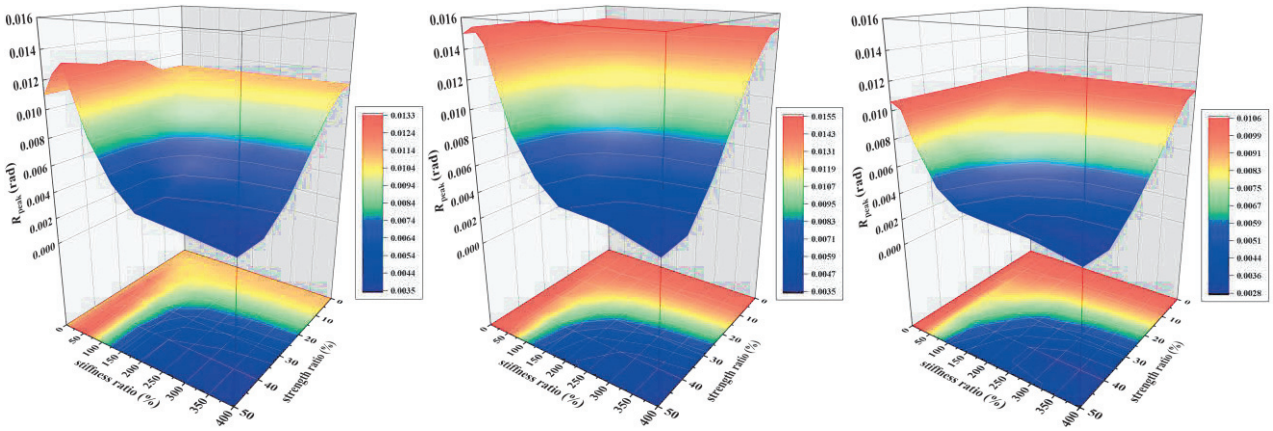

(a) 1st story drift (b) 2nd story drift (c) 3rd story drift

Fig. 5.10. Peak story drift angle of the MA with variations in STS stiffness and strength for el with PGV = 50 cm/s.

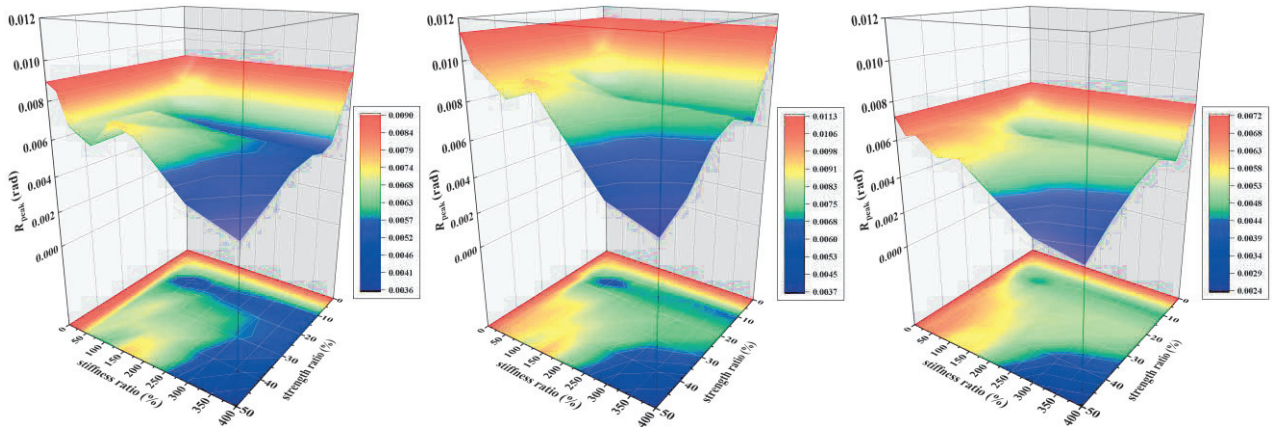

(a) 1st story drift (b) 2nd story drift (c) 3rd story drift

Fig. 5.11. Peak story drift angle of the MA with variations in STS stiffness and strength for taft with PGV = 50 cm/s.

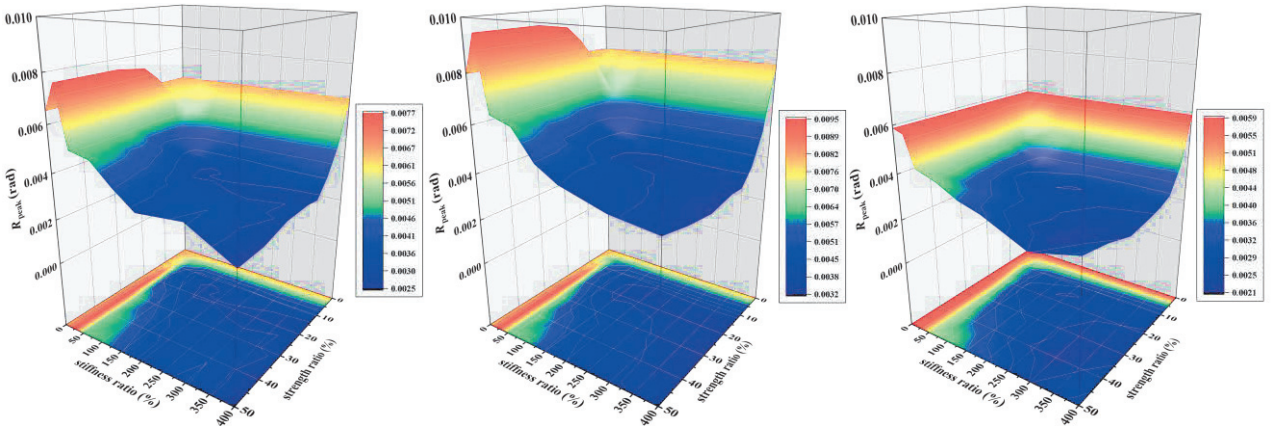

(a) 1st story drift (b) 2nd story drift (c) 3rd story drift

Fig. 5.12. Peak story drift angle of the MA with variations in STS stiffness and strength for hachi with PGV = 50 cm/s.

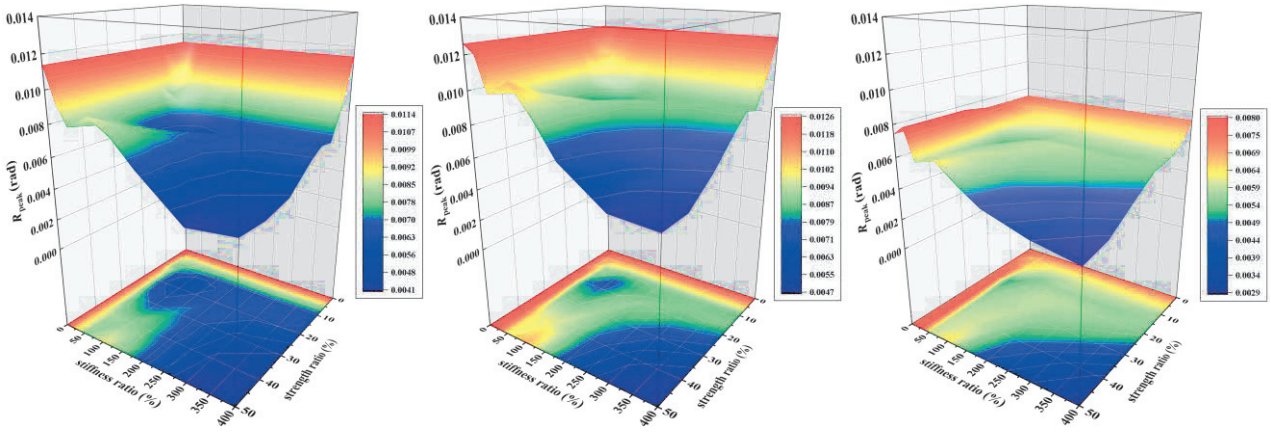

(a) 1st story drift (b) 2nd story drift (c) 3rd story drift

Fig. 5.13. Peak story drift angle of the MA with variations in STS stiffness and strength for kobe with PGV = 50 cm/s.

5.3.4 Influence of upper member width

A schematic of the upper member dimensions is presented in **Fig. 5.14**. As specified in Section 5.2.1, the foundational model maintains a horizontal separation (w_u) of 1200 mm between the two connection points of the braces and the upper member, along with a vertical span (h_u) of 500 mm between the connection points and the rotation center. Furthermore, each story incorporates an STS with a stiffness and strength set at 100% and 20%, respectively, of the corresponding story in the BF.

Fig. 5.15 shows the variation in the amplification factor, stiffness ratio, and strength ratio of the system relative to the bare frame as a function of w_u while maintaining the CSSD and other system parameters constant. The values for these parameters were calculated using Eqs. (2.17), (2.11), and (2.12). With an increase in the distance w_u from 600 to 3600 mm, the amplification factor exhibited a decrease from approximately 5.5 to 2.5. In comparison to the bare frame, the relative stiffness ratio underwent a significant reduction, dropping from 160% to 40%. However, the decline in strength was more gradual, moving from 27% to 12%.

In **Fig. 5.16**, you can observe the maximum story drift angles of the structure as it was tested with different widths of the upper member. The dashed lines in the graph represent the maximum inter-story drift angles of the BF. In the case of the El Centro and Hachinohe earthquake motions, the maximum story drift angle consistently rose with the widening of the upper member. Conversely, for the Taft and Kobe earthquake motions, the maximum inter-story drift angle displayed a pattern of initial decline, followed by an upward trend, across the various widths of the upper member examined.

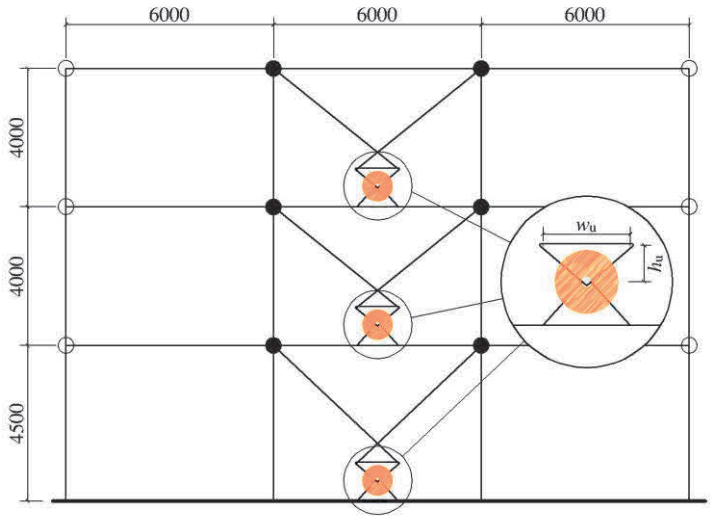

Fig. 5.14. Schematic of the width and height of the upper members.

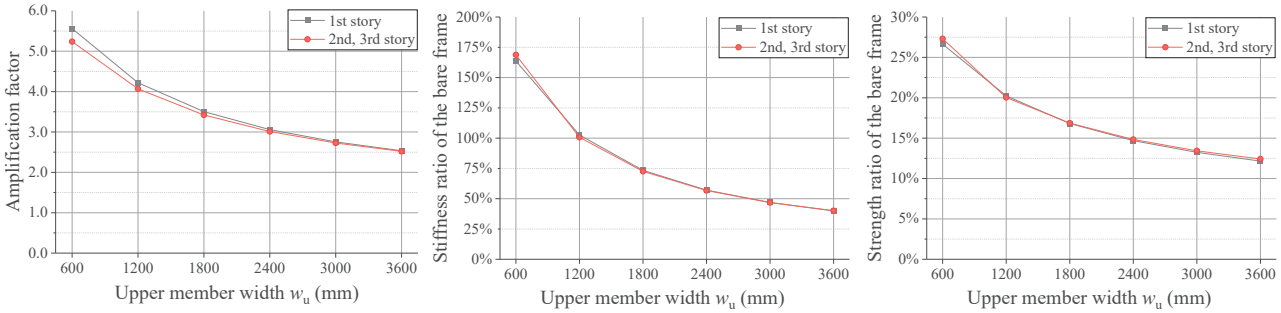

(a) (b) (c)

Fig. 5.15. STS performance with respect to upper member width w_u:
(a) amplification factor, (b) stiffness ratio between STS and bare frame,
(c) strength ratio between STS and bare frame.

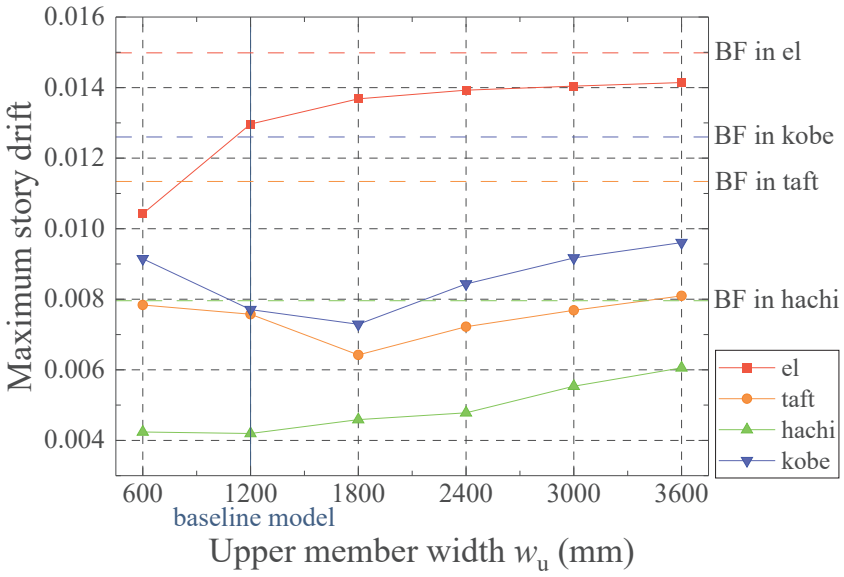

Fig. 5.16. Maximum story drift angle of the MA with various upper member widths for ground motions with PGV = 50 cm/s.

5.3.5 Influence of upper member height

In **Fig. 5.17**, the reduction in the amplification factor, stiffness ratio, and strength ratio of the system relative to the bare frame is presented as the height of the upper member (h_u) is varied from 300 to 1300 mm. This variation was conducted while keeping the CSSD and other system parameters constant. The amplification factor exhibited a decrease from 5 to 2.5, while the relative stiffness ratio and relative strength ratio decreased from around 140% to 40% and 24% to 12%, respectively.

Fig. 5.18 illustrates the maximum story drift angles of the structure as it was tested with different heights of the upper member. The dashed lines in the graph represent the maximum inter-story drift angle of the BF. In the case of the El Centro and Hachinohe earthquake motions, the maximum story drift angle consistently increased with the elevation of the upper member. Conversely, for the Taft

and Kobe earthquake motions, the maximum inter-story drift angles initially decreased and then increased with the various heights of the upper member that were examined.

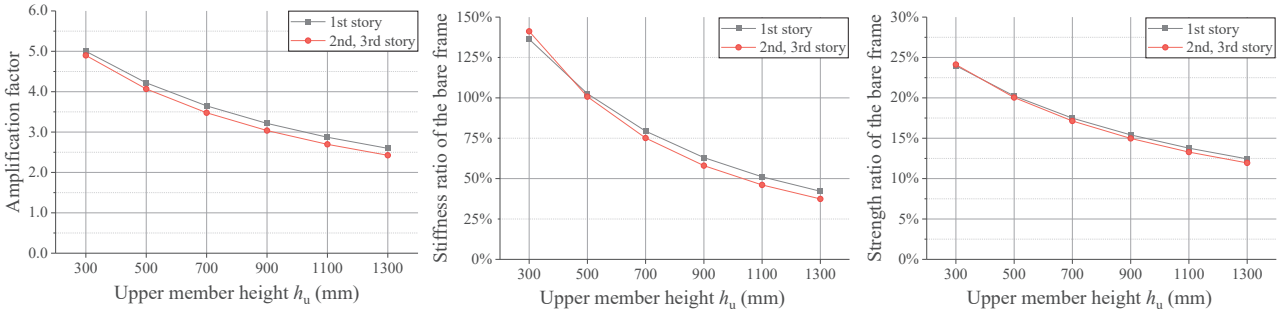

(a) (b) (c)

Fig. 5.17. STS performance with respect to the upper member height h_u: (a) amplification factor, (b) stiffness ratio between STS and bare frame, (c) strength ratio between STS and bare frame.

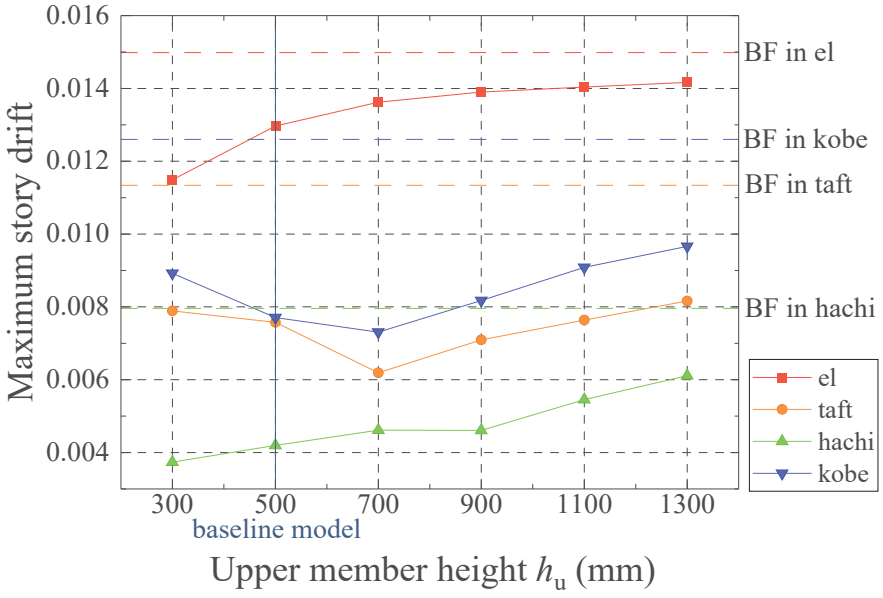

Fig. 5.18. Maximum story drift angle of the MA for various upper member heights for ground motions with PGV = 50 cm/s.

Upon comparing **Figs. 5.16** and **5.18**, a noticeable similarity emerges in the variation of the maximum inter-story drift angle of the MA within the respective ranges of w_u from 600 to 3600 and h_u from 300 to 1300. This consistent pattern stems from analogous variations in the amplification factor, stiffness ratio, and strength ratio of the STS during this process, as depicted in **Figs. 5.15** and **5.17**. As a result, it can be inferred that the MA exhibits a stable seismic performance when subjected to earthquake ground motions, as indicated by the consistent patterns in the amplification factor, system stiffness, and system strength.

5.4 Comparative analysis of diverse STS configurations

5.4.1 Outline of diverse STS configurations

Models B–E were formulated by incorporating various arrangements of a singular damping device at the ground level of a bare frame, as depicted in **Fig. 5.19**. The seesaw-twisting system can be shifted outward from the frame plane by a certain distance to serve as bracing members between the seesaw member and the moment-frame connections across multiple stories, as shown in **Fig. 5.20**. Through the introduction of pretension in the braces, only the tensile force is exerted on the bracing elements, effectively eradicating the issue of brace buckling. This benefit enables the utilization of long steel rods as bracing members between the seesaw member and the moment-frame connections across multiple stories. The effectiveness of such configurations was confirmed in a prior investigation [5]. The vibration tests involving full-scale three-story steel buildings equipped with seesaw systems were executed to showcase their practicality [34].

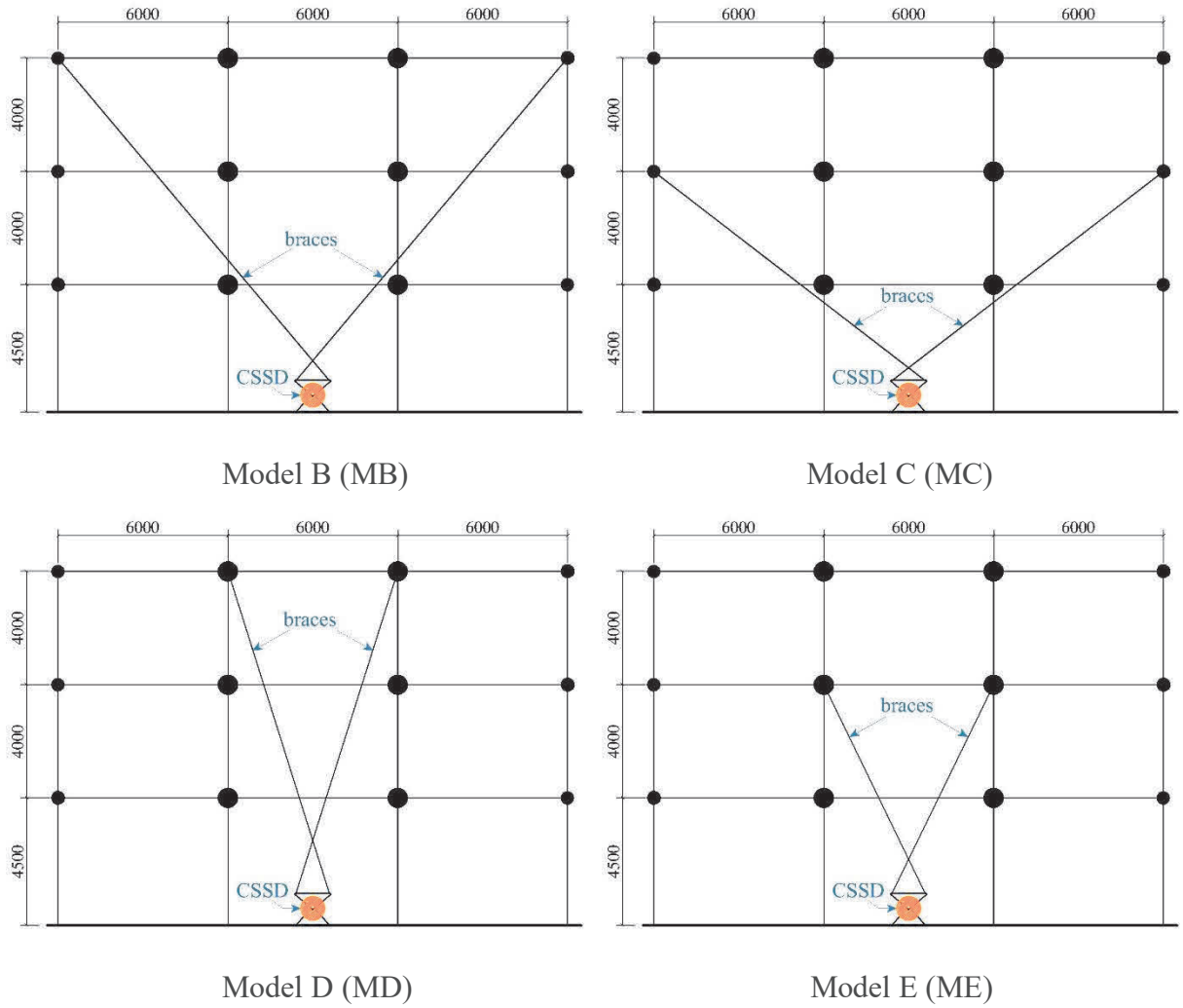

Fig. 5.19. Diverse analysis models.

(a) in experiment[34] (b) in actual engineering practice[40]

Fig. 5.20. Examples of long steel rod bracing for seesaw system.

In Model B, the linkage of bracing members occurred at the uppermost beam-column nodes of the frame, whereas in Model C, this connection took place at the outermost beam-column nodes on the third floor. Models D and E, however, featured bracing member connections at intermediate beam-to-column junctions on the top and third floors, respectively. As depicted in **Figs. 5.21** and **5.22**, the third story of the BF displayed a reduced story drift angle compared to the second story. This consistent characteristic of the top story exhibiting a smaller drift angle guided the specific design of the MC and ME, connecting the bracing members to the beam-column nodes on the third floor. This design choice deliberately excluded the top floor from directly experiencing the damping effect, facilitating a meaningful comparison. To ensure a fair comparison, the CSSD was designed to be identical to that of the first story in the MA, as outlined in Section 5.2.1. The diameters of the bracing members corresponded to those of the MA (90 mm), and the configuration details of the basic damping device remained identical to those of the MA, as illustrated in **Fig. 5.2**. **Table 5** outlines the nomenclature and parameters defining the configurations in the various models, encompassing rod length and stiffness (k_B), angles (α and β), distances (w and e), amplification factor (f_{st}^{p}), and fundamental natural period (T).

5.4.2 Story drift distribution and maximum displacement

Figs. 5.21 and **5.22** illustrate the distribution of peak story drift angles across the six models under four distinct earthquake motions, each with PGV values of 25 and 50 cm/s, respectively. The peak story drift angles presented in these figures represent the maximum drift experienced by the three stories in each model. The introduction of the proposed system consistently resulted in a reduction in

the distribution of inter-story drift in all cases. For earthquake motions featuring a peak ground velocity of 50 cm/s, the MD and ME models displayed larger peak inter-story drift angles. In contrast, the MA, MB, and MC models exhibited smaller peak story drifts. These findings suggest that the MA, MB, and MC models were more effective in mitigating the structural dynamic response. Notably, the MC model showed a larger third-story drift angle compared to the MB model. This difference can be attributed to the fact that the damping system in the MC model is connected to the beam–column nodes of the third floor, with the top story not directly experiencing the damping effect from the STS.

In **Fig. 5.23**, the highest recorded displacement on the uppermost floor of the BF and the models MA–ME, featuring dampers, is showcased. Each STS arrangement contributed to a decrease in the maximum displacement experienced on the top floor. Notably, the MA, MB, and MC demonstrated the most substantial reduction effect compared to all the models subjected to testing.

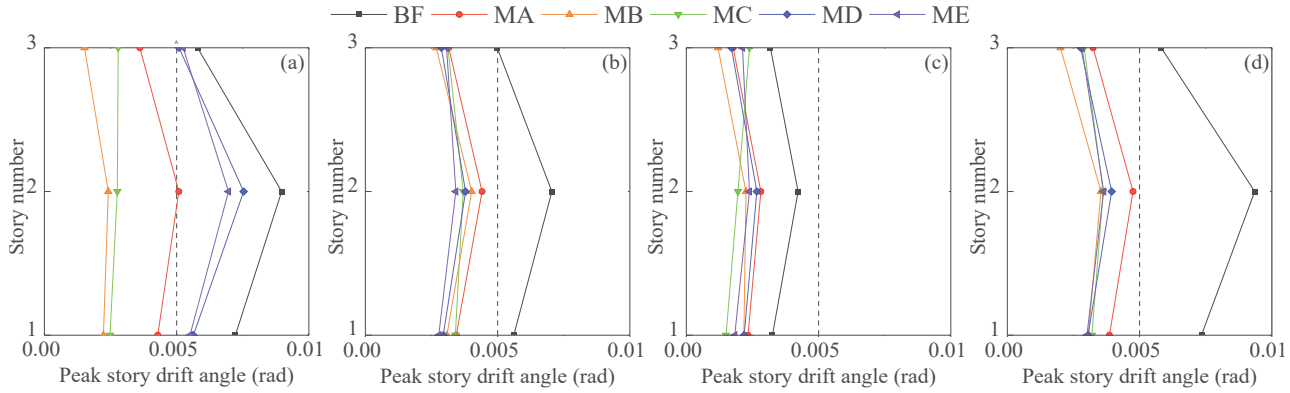

Fig. 5.21. Peak story drift angle for ground motions with PGV = 25 cm/s: (a) el, (b) taft, (c) hachi, and (d) kobe.

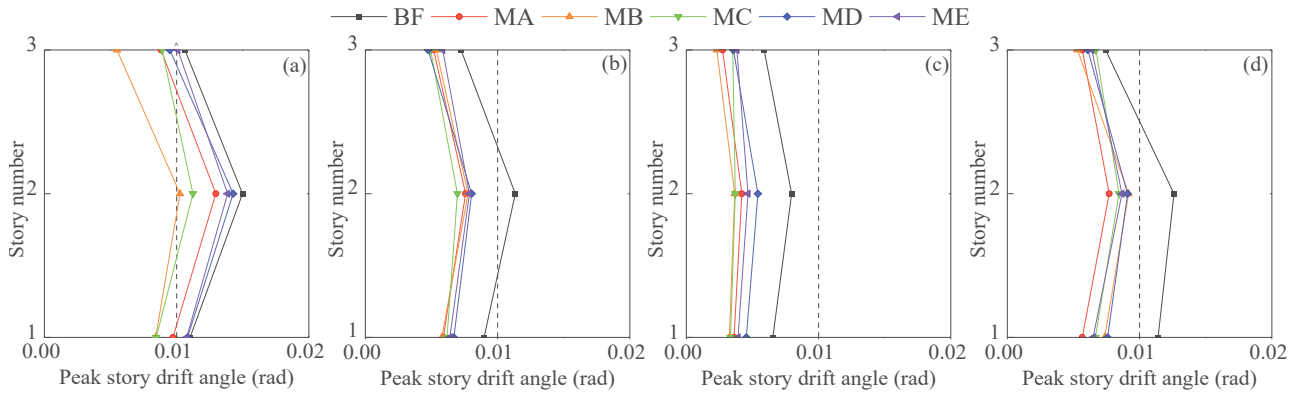

Fig. 5.22. Peak story drift angle for ground motions with PGV = 50 cm/s: (a) el, (b) taft, (c) hachi, and (d) kobe.

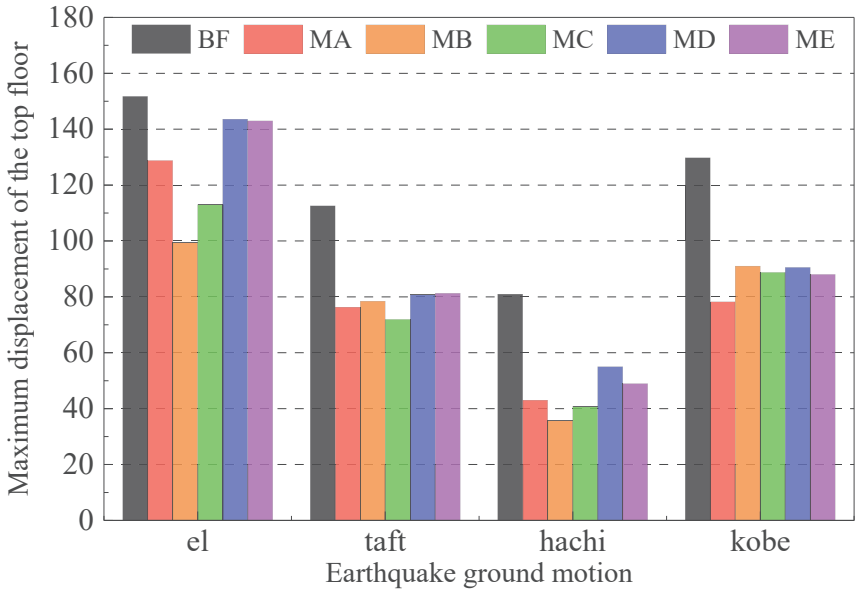

Fig. 5.23. Maximum displacement of the top floor of three-story structures.

5.4.3 Hysteretic curves of the CSSD

In **Fig. 5.24**, the hysteresis curves of the rotational spring, emulating the CSSDs in Models B–E, are portrayed under the El Centro earthquake motion with a PGV of 50 cm/s. The CSSDs exhibited effective operation across all STS configurations. In configurations utilizing a single damping device, the CSSD torsional angles were found to be correlated with the amplification factors (refer to **Table 5**). Notably, the MB and MC, characterized by larger amplification factors, displayed correspondingly larger maximum torsional angles of the CSSD. In contrast, the MD and ME, with smaller amplification factors, demonstrated smaller maximum torsional angles. Furthermore, the MB and MC outperformed the MD and ME in minimizing the story drift angles.

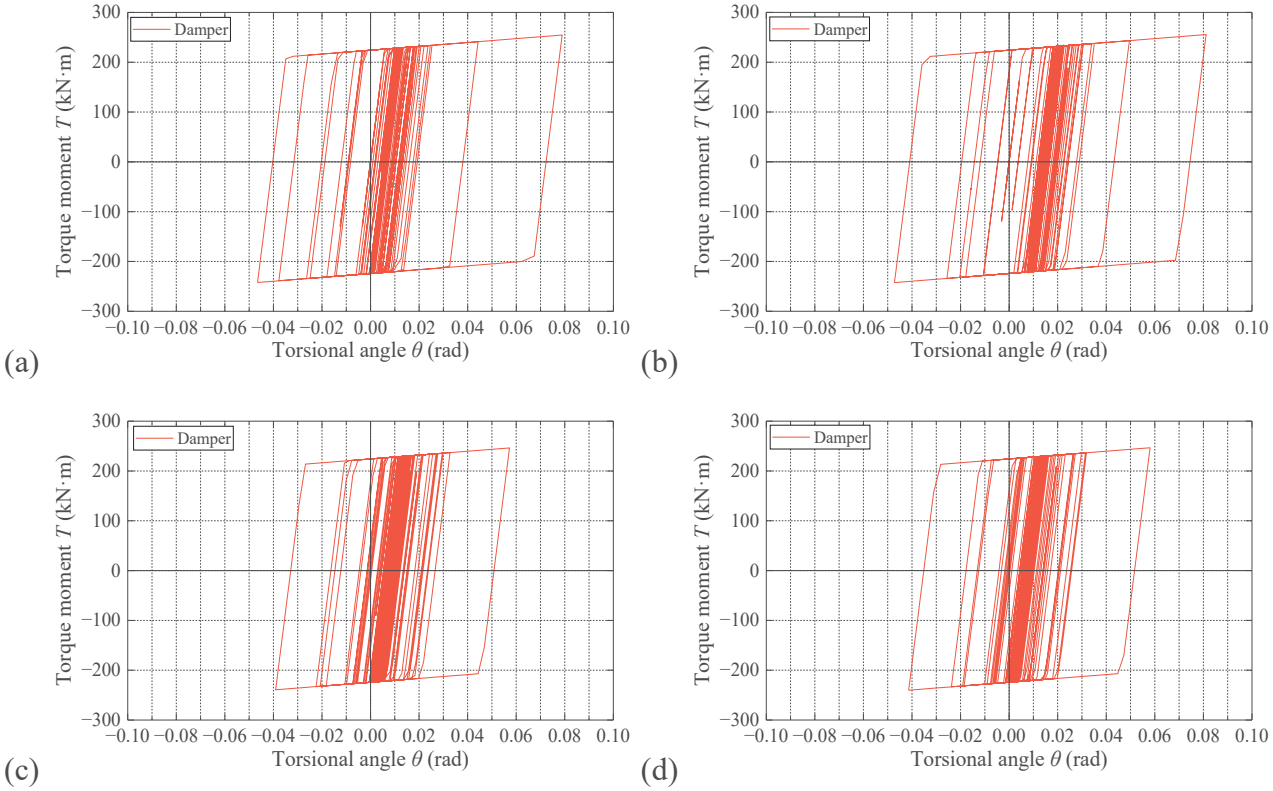

Fig. 5.23. Hysteretic curves of the CSSD for el with PGV=50 cm/s:
(a) MB, (b) MC, (c) MD, and (d) ME.

5.4.4 Plastic hinge formation

Fig. 5.25 presents a visualization of the positions of plastic hinges and their corresponding maximum yield ratios during the seismic response analysis conducted under the Taft earthquake, characterized by a PGV of 50 cm/s. Within the BF, plastic hinges manifested at all beam ends, excluding those of the top-floor beams, and at the bases of all first-story columns. Models equipped with dampers showcased a decrease in both the number and yield ratio of these plastic hinges. Specifically, in the MC model, plastic hinges were confined to the beam ends on the second floor. In the case of MA–MC models, no plastic hinges were observed at the column bases. However, in the MD and ME models, even the two middle column bases exhibited plastic hinges, but compared to the BF, their yield ratios significantly decreased, reaching values slightly greater than 1.

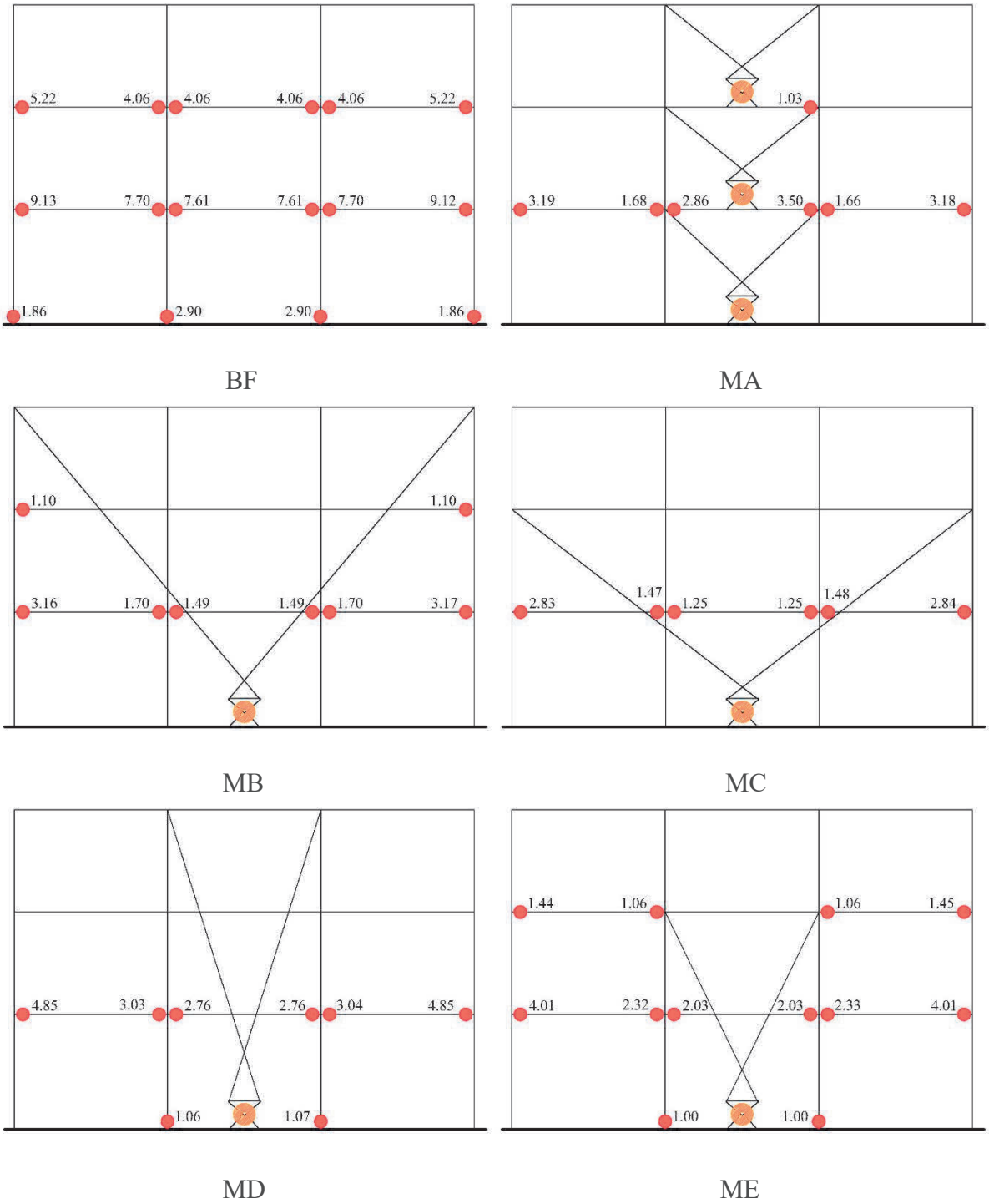

Fig. 5.24. Plastic hinge formation for taft with PGV = 50 cm/s.

6. CONCLUSIONS AND FUTURE RESEARCH

6.1 Experimental and numerical study for STS with CSSD

6.1.1 Conclusions

Sections 3 and 4 featured the introduction of three cyclic loading tests characterized by escalating amplitudes, along with two tests maintaining constant amplitudes. And finite element analyses were conducted on the CSSD, and the key outcomes are outlined below.

- The system exhibited highly stable hysteretic characteristics and a considerable capacity for energy dissipation. Additionally, it's noteworthy that all dampers underwent plastic deformation at a low story drift angle, suggesting the capability for early activation of damper yielding during earthquakes to effectively dissipate energy.
- The experimental specimens demonstrated remarkable resilience, with no failure occurring until they underwent numerous loading cycles and exhibited an exceptional capacity for plastic deformation.
- The force-deformation relationship of the proposed system can be effectively represented by a concise bi-linear model. This model accurately captures both the hysteretic curve and the dissipated energy.
- In terms of the initial lateral stiffness and lateral yield strength, the system performance, as predicted by the theory and finite element analysis, aligned satisfactorily with the experimental findings.
- The performance of the proposed system can be readily manipulated by adjusting the thickness, length, and width of the strips. This allows for independent design of the initial lateral stiffness and lateral yield strength, offering a broad spectrum of variations. Consequently, the proposed system holds the potential to cater to the specific requirements of seismic design practices.

6.1.2 Future research

STS also has the potential to synergistically work with other torsional dampers, such as hydraulic dampers, friction dampers, etc. Exploring these possibilities in future experiments and theoretical studies can contribute valuable insights into the enhanced performance and potentials of combined damper systems.

6.2 Seismic performance of steel structures with STS using CSSD

6.2.1 Conclusions

In Section 5, the seismic response analysis employed four normalized recorded motions. The assessment focused on peak inter-story drift angles for a standard configuration, accounting for variations in beam section, system stiffness and strength, and system specifications. Additionally, an analysis of frames with four distinct STS configurations was conducted to explore peak story drift angles and plastic hinge formation. The key outcomes of this study can be summarized as follows.

- In a standard damper configuration, damping devices are positioned at the midspan of each story (MA), resulting in a commendable damping effect. Generally, as the system's stiffness and strength increase, there is a corresponding decrease in the inter-story drift angle. However, in instances of markedly low stiffness or strength, enhancing either parameter individually has limited influence on reducing the peak story drift.
- In the standard damper arrangement (MA), a notable decrease in the maximum inter-story drift angle was noted when compared to the bare frame, across various studied beam sections, upper member widths (w_u), and heights (h_u). The impact of variations in the beam's cross-section where the damper is situated, upper member width (w_u), and upper member height (h_u) on the maximum inter-story drift angle varies with different earthquake motions. The seismic performance of the MA is contingent upon its amplification factor, system stiffness, and system strength.
- By applying tension to the rods, it becomes feasible to use lengthy steel rods as bracing elements spanning multiple stories, allowing a three-story frame to be outfitted with a single damping system. The effectiveness of connecting the bracing to the outermost beam–column nodes (MB, MC) is superior, while connecting it to the intermediate nodes (MD, ME) results in diminished damping effectiveness. In comparison to connecting the bracing to the top floor (MB, MD), linking it to the third floor (MC, ME) reduces the damping effect of the STS on the top floor.
- All the distinct models incorporate properly functioning CSSDs, effectively reducing the structural dynamic response and minimizing plastic hinge formation. In STS configurations employing a single damping device, the CSSD torsional angle and damping effect showed a positive correlation with the amplification factor. Specifically, when compared to MD and ME models with smaller amplification factors, the MB and MC models, characterized by larger amplification factors, displayed greater maximum torsional angles of the CSSD and more effectively mitigated the inter-story drift angles in the structure.

6.2.2 Future research

In a comprehensive investigation, the seismic performance of the STS was analyzed, utilizing a three-story steel moment frame as a prototype building prototype. Subsequent research endeavors could inquire into exploring the equivalent simplified damper of the STS with CSSD and establishing specific design criteria for this innovative system. This avenue of inquiry holds potential for refining and optimizing the application of the STS in seismic design practices.

REFERENCES

[1] GW Housner, LA Bergman, TK Caughey, AG Chassiakos, et al. Structural control: past, present, and future. Journal of Engineering Mechanics, ASCE 1997;123(9):897–971.

[2] Z Zhang, J Ou, D Li, S Zhang. Optimization design of coupling beam metal damper in shear wall structures. Applied Sciences 2017;7(2):137.

[3] SL Mahyari, HT Riahi, M Hashemi. Investigating the analytical and experimental performance of a pure torsional yielding damper. Journal of Constructional Steel Research 2019;161:385–399.

[4] IH Mualla, B Belev. Performance of steel frames with a new friction damper device under earthquake excitation. Engineering Structures 2002;24:365–371.

[5] JD Kang, H Tagawa. Seismic response of steel structures with seesaw systems using viscoelastic dampers. Earthquake Engineering and Structural Dynamics 2013;42:779–794.

[6] JD Kang, H Tagawa. Seismic performance of steel structures with seesaw energy dissipation system using fluid viscous dampers. Engineering Structures 2013;56:431–442.

[7] J Kim, H Shin. Seismic loss assessment of a structure retrofitted with slit-friction hybrid dampers. Engineering Structures 2017;130:336–350.

[8] SH Oh, YJ Kim, HS Ryu. Seismic performance of steel structures with slit dampers. Engineering Structures 2009;31(9):1997–2008.

[9] H Saffaria, AA Hedayatb, MP Nejad. Post-Northridge connections with slit dampers to enhance strength and ductility dampers to enhance strength and ductility dampers to enhance strength and ductility. Journal of Constructional Steel Research 2013;80(1):138–152.

[10] J Seo, YC Kim, JW Hu. Pilot study for investigating the cyclic behavior of slit damper systems with recentering shape memory alloy (SMA) bending bars used for seismic restrainers. Applied Sciences 2015;5:187–208.

[11] CH Lee, SH Lho, DH Kim, J Oh, YK Ju. Hourglass-shaped strip damper subjected to monotonic and cyclic loadings. Engineering Structures 2016;119(15):122–134.

[12] CH Lee, YK Ju, JK Min, SH Lho, SD Kim. Non-uniform steel strip dampers subjected to cyclic loadings. Engineering Structures 2015;99(15):192–204.

[13] RWK Chan, F Albermani. Experimental study of steel slit damper for passive energy dissipation. Engineering Structures 2008;30:1058–1066.

[14] AA Hedayat. Prediction of the force displacement capacity boundary of an unbuckled steel slit damper. Journal of Constructional Steel Research 2015;114:30–50.

[15] M Aminzadeh, HS Kazemi, SM Tavakkoli. A numerical study on optimum shape of steel slit dampers. Advances in Structural Engineering 2020.

[16] X Ma, E Borchers, A Pena, H krawinkler, S Billington, GG Deierlein. Design and behavior of steel shear plates with openings as energy dissipating fuses. Department of Civil and Environmental Engineering, Stanford University. March, 2010.

[17] Y Liu, Z Guo, X Liu, R Chicchi, B Shahrooz. An innovative resilient rocking column with replaceable steel slit dampers: Experimental program on seismic performance. Engineering Structures 2019;183:830–840.

[18] HA Amiri, EP Najafabadi, HE Estekanchi. Experimental and analytical study of Block Slit Damper. Journal of Constructional Steel Research 2018;141:167–178.

[19] HA Amiri, EP Najafabadi, HE Estekanchi, T Ozbakkaloglu. Performance-based seismic design and assessment of low-rise steel special moment resisting frames with block slit dampers using endurance time method. Engineering Structures 2020;224:110955.

[20] J Lee, J Kim. Development of box-shaped steel slit dampers for seismic retrofit of building structures. Engineering Structures 2017;150:934–946.

[21] A Naeem, J Kim. Seismic performance evaluation of a multi-slit damper. Engineering Structures 2019;189:332–346.

[22] A Naeem, MN Eldin, J Kim, J Kim. Seismic Performance Evaluation of a Structure Retrofitted Using Steel Slit Dampers with Shape Memory Alloy Bars. International Journal of Steel Structures 2017;17(4):1627–1638.

[23] JD Kang, H Tagawa. Comparison between experimental and analytical results for seesaw energy dissipation systems using fluid viscous dampers. Earthquake Engineering and Engineering Vibration 2016;15:79–90.

[24] PS Katsimpini, GA Papagiannopoulos. Effectiveness of the Seesaw System as a Means of Seismic Upgrading in Older, Non-Ductile Reinforced Concrete Buildings. Vibration 2023;6(1):102–112.

[25] H Tagawa, J Gao. Evaluation of vibration control system with U-dampers based on quasi-linear motion mechanism. Journal of Constructional Steel Research 2012;70:213–225.

[26] H Tagawa, T Yamanishi, A Takaki, RWK Chan. Cyclic behavior of seesaw energy dissipation system with steel slit dampers. Journal of Constructional Steel Research 2016;117:24–34.

[27] PS Katsimpini, GA Papagiannopoulos, MG Sfakianakis. On the seismic response and damping capacity of low-rise plane steel frames with seesaw system. Soil Dynamics and Earthquake Engineering 2018;107:407–416.

[28] PS Katsimpini, GA Papagiannopoulos, PK Askouni, DL Karabalis. Seismic response of low-rise 3-D steel structures equipped with the seesaw system. Soil Dynamics and Earthquake Engineering 2020;128:105877.

[29] PS Katsimpini, PK Askouni, GA Papagiannopoulos, DL Karabalis. Seismic drift response of seesaw-braced and buckling-restrained braced steel structures: A comparison study. Soil Dynamics and Earthquake Engineering 2020;129:105925.

[30] XF Sun. Mechanics of materials. Fifth Edition. Higher Education Press 2009 (in Chinese).

[31] Practical Structural Design for High-Rise Buildings. The Building Center of Japan 2007 (in Japanese).

[32] SH Oh, YJ Kim, HS Ryu. Seismic performance of steel structure with slit dampers. Engineering Structures 2009;31:1997–2008.

[33] Recommended Provisions for Seismic Damping Systems applied to Steel Structures. Architectural Institute of Japan 2014 (in Japanese) .

[34] Y Hirata, H Tagawa, M Kawashima, H Harada. Experimental study on practical application of seesaw system. Proceedings of the fib Symposium of Concrete Structures: New Trends for Eco-Efficiency and Performance, Virtual, Lisbon, 2021;2067–2076.

[35] FEMA 461. Interim testing protocols for determining the seismic performance characteristics of structural and nonstructural components. Redwood City, California: Applied Technology Council; 2007.

[36] Sheldon Imaoka. Chaboche nonlinear kinematic hardening model. STI0805, ANSYS Release: 11, 2008.

[37] S Feng, H Tagawa, X Chen. Seesaw-twisting system with cylindrical steel slit damper for vibration control of structures. Structures 2023;50:1376–1390.

[38] S Feng, H Tagawa, X Chen. Experimental study of cylindrical steel slit damper for passive energy dissipation. In: Proceedings of the 3rd International Civil Engineering and Architecture Conference, Kyoto, Japan, 2023.

[39] Open system for earthquake engineering simulation (OpenSees) ver. 3.0.3. Available from: http://opensees.berkeley.edu/ (last accessed July. 2023).

[40] Application of "vibration control system" in an actual structure, Sumitomo Mitsui Construction, https://www.smcon.co.jp/topics/2022/09091300/.

APPENDIX A. DETERMINATION OF C_1 AND C_2 FOR BI-LINEAR MODELS

Fig. A.1 presents examples of the differences in dissipated energy at the amplitude points, where y_i and h_i denote the dissipated energies obtained from the loading tests and bilinear models.

The absolute difference in total energy dissipation at the maximum considered amplitude of 0.02 rad is obtained from:

$$E_{\text{total}} = \left|h_{-0.02}^{2\text{nd}} - y_{-0.02}^{2\text{nd}}\right| \quad (\text{A. 1})$$

where, $h_{-0.02}^{2\text{nd}}$ refers to the dissipated energy of the test until the second cycle at –0.02 rad amplitude.

The sum of the absolute differences at all the amplitude points till 0.02 rad is obtained from:

$$\begin{aligned} E_{\text{sum}} = {} & |h_{0.005}^{1\text{st}} - y_{0.005}^{1\text{st}}| + |h_{-0.005}^{1\text{st}} - y_{-0.005}^{1\text{st}}| + \left|h_{0.005}^{2\text{nd}} - y_{0.005}^{2\text{nd}}\right| + \left|h_{-0.005}^{2\text{nd}} - y_{-0.005}^{2\text{nd}}\right| \\ & + |h_{0.01}^{1\text{st}} - y_{0.01}^{1\text{st}}| + |h_{-0.01}^{1\text{st}} - y_{-0.01}^{1\text{st}}| + \left|h_{0.01}^{2\text{nd}} - y_{0.01}^{2\text{nd}}\right| + \left|h_{-0.01}^{2\text{nd}} - y_{-0.01}^{2\text{nd}}\right| \\ & + |h_{0.015}^{1\text{st}} - y_{0.015}^{1\text{st}}| + \left|h_{-0.015}^{2\text{nd}} - y_{-0.015}^{2\text{nd}}\right| + \left|h_{0.015}^{2\text{nd}} - y_{0.015}^{2\text{nd}}\right| + \left|h_{-0.015}^{2\text{nd}} - y_{-0.015}^{2\text{nd}}\right| \\ & + |h_{0.02}^{1\text{st}} - y_{-0.02}^{1\text{st}}| + \left|h_{-0.02}^{2\text{nd}} - y_{-0.02}^{2\text{nd}}\right| + \left|h_{0.02}^{2\text{nd}} - y_{0.02}^{2\text{nd}}\right| \\ & + \left|h_{-0.02}^{2\text{nd}} - y_{-0.02}^{2\text{nd}}\right| \quad (\text{A. 2}) \end{aligned}$$

The dissipated energy differences, E_{total} and E_{sum} vary for different values of c_1 and c_2. Figs. A. 2, A. 3, and A. 4 show the variations in E_{total} and E_{sum} for three test specimens. Overall, the energy differences exhibited a downward convex change trend for E_{total} and E_{sum}. Based on the energy dissipation differences and agreement of the hysteretic curves, c_1=0.23, 0.11, and 0.14 were selected for specimens T-A, T-B, and T-C, respectively, and c_2=0.01 was determined for the three specimens.

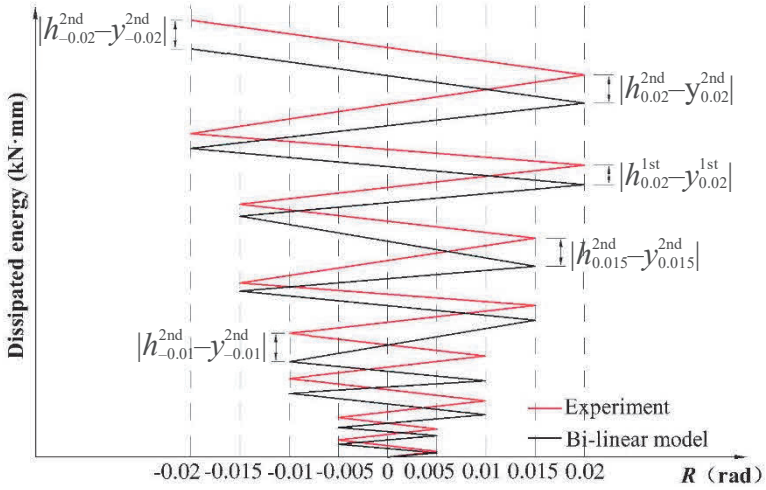

Fig. A.1. Examples of absolute differences at the amplitude points.

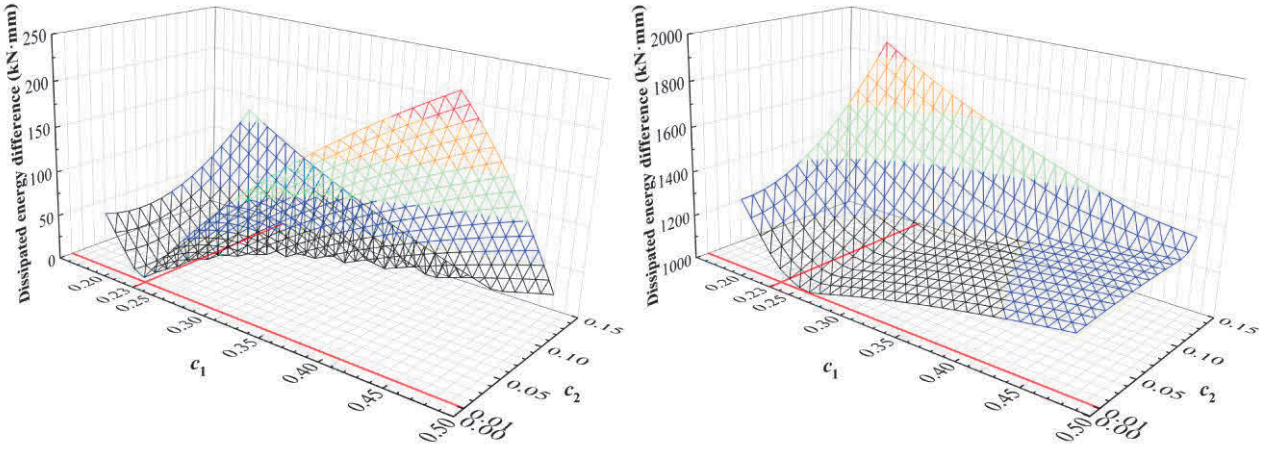

(a) E_{total} (b) E_{sum}

Fig. A.2. Dissipated energy difference for T-A.

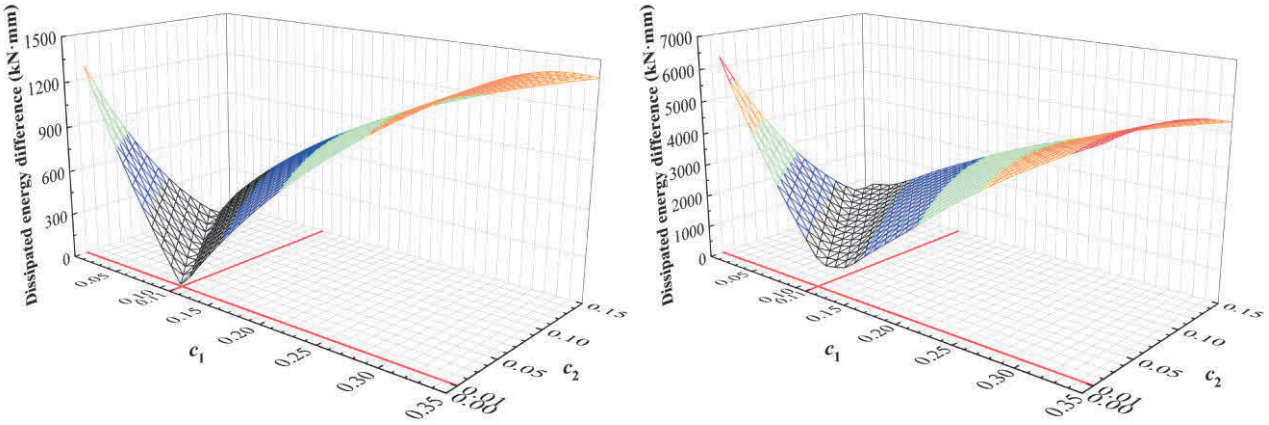

(a) E_{total} (b) E_{sum}

Fig. A.3. Dissipated energy difference for T-B.

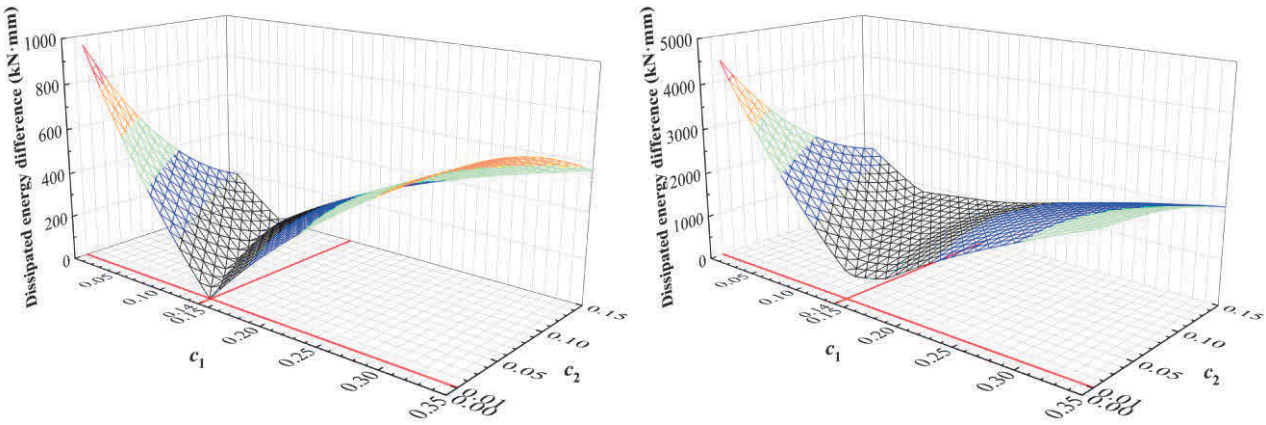

(a) E_{total} (b) E_{sum}

Fig. A.4. Dissipated energy difference for T-C.

RELATED PUBLICATIONS

1. S Feng, H Tagawa, X Chen. Seesaw-twisting system with cylindrical steel slit damper for vibration control of structures. Structures 2023;50:1376–1390.

2. Experimental study of cylindrical steel slit damper for passive energy dissipation. S Feng, H Tagawa, X Chen. In: Proceedings of the 3rd International Civil Engineering and Architecture Conference, Kyoto, Japan, March 17th to 20th, 2023.

3. S Feng, H Tagawa, X Chen. Seismic performance of steel structures with seesaw-twisting system using cylindrical steel slit damper. Structures 2023;58:105422.